

This work is on a Creative Commons Attribution 4.0 International (CC BY 4.0) license, <https://creativecommons.org/licenses/by/4.0/>. Access to this work was provided by the University of Maryland, Baltimore County (UMBC) ScholarWorks@UMBC digital repository on the Maryland Shared Open Access (MD-SOAR) platform.

Please provide feedback

Please support the ScholarWorks@UMBC repository by emailing scholarworks-group@umbc.edu and telling us what having access to this work means to you and why it's important to you. Thank you.

THE 2019 OUTBURST OF THE 2005 CLASSICAL NOVA V1047 CEN:
A RECORD BREAKING DWARF NOVA OUTBURST OR A NEW PHENOMENON?

E. AYDI,¹ K. V. SOKOLOVSKY,^{1,2} J. S. BRIGHT,³ E. TREMOU,⁴ M. M. NYAMAI,⁵ A. EVANS,⁶ J. STRADER,¹ L. CHOMIUK,¹
G. MYERS,⁷ F.-J. HAMBSCH,^{8,9,10} K. L. PAGE,¹¹ D. A. H. BUCKLEY,^{12,5} C. E. WOODWARD,¹³ F. M. WALTER,¹⁴
P. MRÓZ,^{15,16} P. J. VALLELY,¹⁷ T. R. GEBALLE,¹⁸ D. P. K. BANERJEE,¹⁹ R. D. GEHRZ,¹³ R. P. FENDER,^{3,5}
M. GROMADZKI,¹⁶ A. KAWASH,¹ C. KNIGGE,²⁰ K. MUKAI,^{21,22} U. MUNARI,²³ M. ORIO,^{24,25} V. A. R. M. RIBEIRO,^{26,27}
J. L. SOKOLOSKI,²⁸ S. STARRFIELD,²⁹ A. UDALSKI,¹⁶ AND P. A. WOUTD⁵

- ¹Center for Data Intensive and Time Domain Astronomy, Department of Physics and Astronomy, Michigan State University, East Lansing, MI 48824, USA
²Sternberg Astronomical Institute, Moscow State University, Universitetskii pr. 13, 119992 Moscow, Russia
³Astrophysics, Department of Physics, University of Oxford, Keble Road, Oxford, OX1 3RH, UK
⁴LESIA, Observatoire de Paris, CNRS, PSL, SU/UPD, Meudon, France
⁵Department of Astronomy, University of Cape Town, Private Bag X3, Rondebosch 7701, South Africa
⁶Astrophysics Group, Keele University, Keele, Staffordshire, ST5 5BG, UK
⁷American Association of Variable Star Observers, 5 Inverness Way, Hillsborough, CA 94010
⁸Vereniging Voor Sterrenkunde (VVS), Oostmeers 122 C, 8000 Brugge, Belgium
⁹Groupe Européen d'Observations Stellaires (GEOS), 23 Parc de Levesville, 28300 Bailleau l'Evêque, France
¹⁰Bundesdeutsche Arbeitsgemeinschaft für Veränderliche Sterne (BAV), Munsterdamm 90, 12169 Berlin, Germany
¹¹School of Physics & Astronomy, University of Leicester, LE1 7RH, UK
¹²South African Astronomical Observatory, P.O. Box 9, 7935 Observatory, South Africa
¹³Minnesota Institute for Astrophysics, School of Physics & Astronomy, 116 Church Street SE, University of Minnesota, Minneapolis, MN 55455, USA
¹⁴Department of Physics & Astronomy, Stony Brook University, Stony Brook, NY 11794-2100 USA
¹⁵Division of Physics, Mathematics, and Astronomy, California Institute of Technology, Pasadena, CA 91125, USA
¹⁶Astronomical Observatory, University of Warsaw, Al. Ujazdowskie 4, 00-478 Warszawa, Poland
¹⁷Department of Astronomy, The Ohio State University, 140 West 18th Avenue, Columbus, OH 43210, USA
¹⁸Gemini Observatory/NSF's NOIRLab, 670 N. Aōhoku Place Hilo, Hawaii, 96720, USA
¹⁹Physical Research Laboratory, Navrangpura, Ahmedabad, Gujarat 380009, India
²⁰School of Physics and Astronomy, University of Southampton, Highfield, Southampton, SO17 1BJ, UK
²¹CRESST II and X-ray Astrophysics Laboratory, NASA/GSFC, Greenbelt, MD 20771, USA
²²Department of Physics, University of Maryland, Baltimore County, 1000 Hilltop Circle, Baltimore, MD 21250, USA
²³INAF Astronomical Observatory of Padova, 36012 Asiago (VI), Italy
²⁴INAF-Osservatorio di Padova, vicolo dell'Osservatorio 5, I-35122 Padova, Italy
²⁵Department of Astronomy, University of Wisconsin, 475 N. Charter St., Madison, WI 53704, USA
²⁶Instituto de Telecomunicações, Campus Universitário de Santiago, 3810-193 Aveiro, Portugal
²⁷Departamento de Física, Universidade de Aveiro, Campus Universitário de Santiago, 3810-193 Aveiro, Portugal
²⁸Columbia Astrophysics Laboratory and Department of Physics, Columbia University, New York, NY 10027, USA
²⁹School of Earth and Space Exploration, Arizona State University Tempe, AZ 85287-1404, USA

(Received ***; Revised ***; Accepted ***)

Submitted to ApJ

ABSTRACT

We present a detailed study of the 2019 outburst of the cataclysmic variable V1047 Cen, which hosted a classical nova eruption in 2005. The peculiar outburst occurred 14 years after the classical nova event, lasted for more than 400 days, and reached an amplitude of around 6 magnitudes in the optical. Early spectral follow-up revealed what could be a dwarf nova (accretion disk instability) outburst in a classical nova system. However, the outburst duration, high velocity ($>2000 \text{ km s}^{-1}$) features in the optical line profiles, luminous optical emission, and the presence of prominent long-lasting radio emission, together suggest a phenomenon more exotic and energetic than a dwarf nova outburst.

There are striking similarities between this V1047 Cen outburst and those of “combination novae” in classical symbiotic stars. We suggest that the outburst may have started as a dwarf nova that led to the accretion of a massive disk, which in turn triggered enhanced nuclear shell burning on the white dwarf and eventually led to generation of a wind/outflow. From optical photometry we find a *possible* orbital period of 8.36 days, which supports the combination nova scenario and makes the system an intermediate case between typical cataclysmic variables and classical symbiotic binaries. If true, such a phenomenon would be the first of its kind to occur in a system that has undergone a classical nova eruption and is intermediate between cataclysmic variables and symbiotic binaries.

Keywords: stars: novae, cataclysmic variables — white dwarfs.

1. INTRODUCTION

Cataclysmic Variables (CVs) are interacting binary systems, each consisting of a white dwarf accreting material from a Roche-lobe-filling companion. The material flowing from the companion forms an accretion disk around the white dwarf before being dumped on its surface. In the case of a highly-magnetized white dwarf ($B > 10^6$ G), the magnetic field of the white dwarf truncates the inner regions of the disk or even completely prevents it from being formed. In this case the material follows the magnetic field lines onto the surface of the white dwarf. These are known as magnetic CVs (see Warner 1995 for a review). CVs experience several types of cataclysmic events and thermonuclear explosions, hence the name. One of these events is called a dwarf nova (DN) and is a viscosity-induced instability in the accretion disk, resulting in a temporary increase in mass transfer rate and heating the whole disk. DNe manifest as relatively low amplitude outbursts, typically $\Delta m \sim 2 - 5$ mag up to $\sim 9 - 10$ mag in some extreme cases (Kawash et al. 2021).

While material builds up on the surface of the white dwarf through secular accretion, the pressure and density increases in its surface layers. Once a critical density is reached, a thermonuclear runaway is triggered on the surface of the white dwarf, leading to an increase in the brightness of the system by up to 15 mag or more in a matter of a few days (Starrfield et al. 1972; Yaron et al. 2005). These events are known as classical novae (see Gallagher & Starrfield 1978; Bode & Evans 2008; Wou 2014; Della Valle & Izzo 2020; Chomiuk et al. 2020 for reviews) and their recurrence timescale is typically \gtrsim thousands of years (Yaron et al. 2005). In some cases, novae recur on shorter timescales – short enough to be recorded more than once. These are called recurrent novae and these systems are usually characterized by a high mass transfer rate, often due to the presence of an evolved secondary (Schaefer 2010).

After a classical nova event, the mass transfer rate is expected to be high enough to keep the disk in a hot, ionized state, temporarily preventing DNe in the system. DNe are only expected thousands of years later, when the mass transfer rate becomes low enough for the disk to cool and again become susceptible to disk instability events. This is implied by the hibernation scenario of CVs (Shara et al. 1986), which suggests that CVs go through cycles of low and high states of mass transfer rate. In this scenario, the states are mostly determined by the irradiation of the secondary by a nova event (which increases the mass transfer rate) and the growing separation between the two stars (which decreases the mass transfer rate). Only a few CV systems have

shown DN outbursts after classical nova eruptions; e.g., GK Per (Sabbadin & Bianchini 1983; Bianchini et al. 1986), V1017 Sgr (Sekiguchi 1992; Salazar et al. 2017), and V446 Her (Honeycutt et al. 1995, 2011).

1.1. V1047 Cen – the 2019 outburst

V1047 Cen (Nova Cen 2005) was discovered as a Galactic transient on 2005 September 1.03 at a visual magnitude of around 8.5 (left panel of Figure 1) and later classified spectroscopically as a classical nova eruption (Liller et al. 2005). Walter et al. (2012) reported spectroscopic follow up taken approximately 5 and 7 days after discovery. The spectra showed typical lines of Balmer, Fe II, and [O I], which are characteristic of a classical nova near optical peak. The Balmer lines showed multiple P Cygni absorptions with blueshifted velocities of around 750 and 1800 km s⁻¹.

Otherwise, V1047 Cen was not extensively observed during the 2005 eruption and little else is known about the classical nova eruption. Archival observations of the system taken by the Inner Galactic Disk with MIPS (MIPSGAL; Carey et al. 2009) Survey in the 24 and 70 micron bands, yield a 24-micron average magnitude of 0.72 ± 0.02 mag (Gutermuth & Heyer 2015). The MIPSGAL survey data were collected between September 2005 and October 2006. Additional archival observations by the VISTA Variables in the Via Lactea (VVV) survey between March 2010 and August 2011, show the nova fading from $K=12.84$ to $K=13.11$ (Saito et al. 2012). The Neil Gehrels Swift Observatory (hereafter *Swift*; Gehrels et al. 2004) observed the classical nova eruption between 2005 and 2008 (Ness et al. 2007). The observations obtained in November 2005 and January 2006 resulted in detections of hard X-rays from strongly absorbed shock emission, which are typically seen in novae during the early weeks/months of the eruption (see, e.g., Mukai et al. 2008; Schwarz et al. 2011; Gordon et al. 2021). The *Swift* observations obtained in 2008 led to a non-detection.

Fourteen years after the 2005 nova eruption, Delgado et al. (2019) reported the discovery of an astronomical transient AT2019hik/Gaia19cfn possibly associated with V1047 Cen on 2019 June 11.6, with a discovery magnitude of 16.2 in the *G*-band. Based on regular monitoring by the Optical Gravitational Lensing Experiment (OGLE; Udalski et al. 2015) survey, Mroz & Udalski (2019) confirmed that the FK5 J2000 equatorial coordinates of the transient ($[\alpha, \delta] = [13^{\text{h}}20^{\text{m}}49^{\text{s}}.78, -62^{\circ}37'50''6]$) were consistent with those of V1047 Cen and found that the re-brightening of the system started as early as 2019 April 6.11 (HJD 2458579.61; right panel of Figure 1). This date is considered as the out-

burst start (t_0) throughout this paper. Mroz & Udalski (2019) noted that the slow re-brightening of the system is inconsistent with a recurrent nova eruption. The re-brightening of the system triggered follow-up observations across the electromagnetic spectrum. Aydi et al. (2019) reported optical spectroscopy, which showed DN outburst spectral features superimposed on spectral features of a classical nova nebula. Geballe et al. (2019) reported infrared spectroscopy of the then ongoing outburst, during its first 160 days, concluding that the event was possibly a DN outburst. However, upon further follow-up, the 2019 outburst of V1047 Cen seems to be a more exotic phenomenon.

Here we report on multi-wavelength follow-up of the 2019 outburst of V1047 Cen spanning the spectrum from X-ray to radio. In Section 2 we present the observations and data reduction. In Section 3 we show our results, while in Section 4 we offer discussion about the nature of the event and its peculiar observational features. Our conclusions are given in Section 5.

2. OBSERVATIONS AND DATA REDUCTION

2.1. Optical and near-IR photometry

V1047 Cen has been observed by the OGLE sky survey (Udalski et al. 2015) since May 2013, several years before the outburst, as part of the OGLE Galaxy Variability Survey (GVS). All data were taken in the I band with an exposure time of 30 s, and they were reduced and calibrated using the standard OGLE pipeline (Udalski et al. 2015). A sample of the observations is listed in Table A.1.

Optical photometry between days 76 and 437 was performed in the $BVRI$ bands by several observers from the American Association of Variable Star Observers (AAVSO; Kafka 2020). The bulk of the multi-band photometry comes from two observers, Gordon Meyer and Josch Hamsch. A sample of the observations is listed in Table A.2.

We obtained SMARTS *Andicam* photometry in the J , H , and K_s bands on 29 nights between days 80 and 117. Data reduction is described in Walter et al. (2012). A sample of the observations is listed in Table A.3. The *Andicam* instrument was retired on 2019 August 1 (day 117). We also make use of IR photometry from the enhanced Wide-field Infrared Survey Explorer (NEOWISE; Mainzer et al. 2011) covering only three epochs during the outburst in the $W1$ ($3.35\ \mu\text{m}$) and $W2$ ($4.60\ \mu\text{m}$) bands. A log of the observations is listed in Table A.4.

The field of V1047 Cen was observed by the Transiting Exoplanet Survey Satellite (*TESS*; Ricker et al. 2015) during sector 11, which covers the early rise of the 2019

outburst between days 17 and 44. We used the open-source tool ELEANOR (Feinstein et al. 2019) to extract light curves from the *TESS* full-frame images, opting to utilize the corrected flux light curve and to only include data that are not associated with a quality flag.

All the data will be available as online material. All multi-band photometry is calibrated using the *Vega* system zero points.

2.2. Optical and IR spectroscopy

We obtained optical and IR spectroscopic observations of the 2019 outburst between days 74 and 643 using a diverse group of telescopes and instruments. A log of the spectral observations is presented in Table A.5.

We obtained spectra using the High Resolution Spectrograph (HRS; Barnes et al. 2008; Bramall et al. 2010, 2012; Crause et al. 2014) and the Robert Stobie Spectrograph (RSS; Burgh et al. 2003; Kobulnicky et al. 2003) mounted on the Southern African Large Telescope (SALT; Buckley et al. 2006; O’Donoghue et al. 2006) in Sutherland, South Africa. HRS was used in the low resolution LR mode, yielding a resolving power $R \approx 14,000$ over the range 4000–9000 Å. The primary reduction of the HRS spectroscopy was conducted using the SALT science pipeline (Crawford et al. 2010), which includes over-scan correction, bias subtraction, and gain correction. The rest of the reduction was done using the MIDAS FEROS (Stahl et al. 1999) and *echelle* (Ballester 1992) packages. The reduction procedure is described by Kniazev et al. (2016). RSS was used in long-slit mode with the 1.5 arcsec slit and the PG900 grating, resulting in a resolving power $R \approx 1500$. The spectra were first reduced using the PySALT pipeline (Crawford et al. 2010), which involves bias subtraction, cross-talk correction, scattered light removal, bad pixel masking, and flat-fielding. The wavelength calibration, background subtraction, and spectral extraction were done using the Image Reduction and Analysis Facility (IRAF; Tody 1986).

We also carried out low- and medium-resolution optical spectroscopy using the Goodman spectrograph (Clemens et al. 2004) on the 4.1 m Southern Astrophysical Research (SOAR) telescope located on Cerro Pachón, Chile. The observations were carried out in two setups: one setup using the $400\ \text{mm}^{-1}$ grating and a $0.95''$ slit, yielding a resolving power $R \approx 1000$ over the wavelength range 3820–850 Å. Another setup was used with a $2100\ \text{mm}^{-1}$ grating and a $0.95''$ slit, yielding a resolving power $R \approx 5000$ in a region centered on $H\alpha$ that is $570\ \text{Å}$ wide. The spectra were reduced and optimally extracted using the APALL package in IRAF.

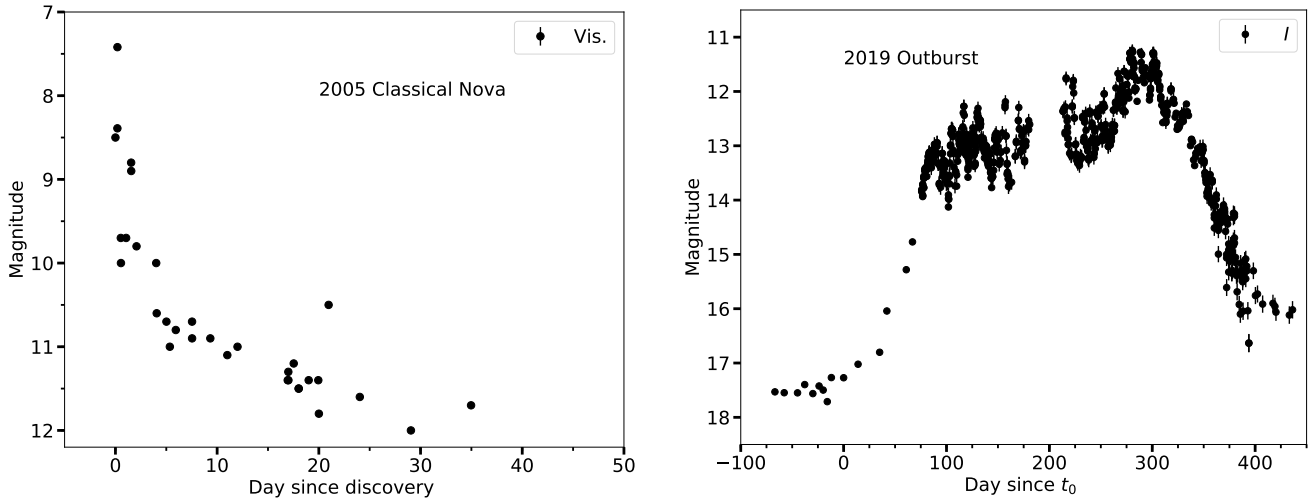


Figure 1. A direct comparison between the visual light curve of the 2005 classical nova eruption from AAVSO (*left*) and the OGLE *I*-band light curve of the 2019 outburst (*right*). The remarkable difference between the two light curves indicates that the two events are of a completely different nature.

Four high-resolution spectra were also obtained using the Chiron fiber-fed echelle spectrograph (Tokovinin et al. 2013) mounted on the CTIO 1.5m telescope. Integration times were 20 minutes, with three integrations per night summed for 1 hour net exposure time. All spectra were taken in “fiber mode”, with 4x4 on-chip binning yielding a resolving power $\lambda/\delta\lambda \approx 27,800$. The data were reduced using a pipeline coded in IDL (Walter 2017)¹.

2.3. Infrared spectroscopy

Near-infrared spectra of V1047 Cen were obtained at the Gemini South Telescope on Cerro Pachon in Chile on days 223 and 230 using the facility instrument FLAMINGOS-2, for program GS-2020A-Q-201. The observations are summarized in Table A.6,. The 0.36” wide slit and R3000 grism were employed to obtain spectra at resolving powers, R , of up to 3000 in portions of the *J*, *H*, and *K* windows. The JH R1200 grism was used with the same slit to obtain a spectrum covering 0.89-1.75 μm . Note that for each grism there is considerable variation in R across each wavelength interval. (see Ref.²). Data reduction employed standard near-infrared techniques utilizing both Gemini/IRAF and Figo commands (Shortridge et al. 1992). Flux calibrations, derived from spectra of the standard stars listed in Table A.6 and are accurate to $\pm 30\%$.

¹ http://www.astro.sunysb.edu/fwalter/SMARTS/CHIRON/ch_reduce.pdf

² <http://www.gemini.edu/instrumentation/flamingos-2/components#Grisms>

NASA SOFIA (Stratospheric Observatory for Infrared Astronomy; Young et al. 2012) airborne observations of V1047 Cen were obtained with the the Faint Object InfraRed CAMERA (FORCAST; Herter et al. 2018), the dual-channel mid-infrared imager and grism spectrometer operating from 5 to 40 μm on two separate, consecutive flight series on 2019 July 02.542 UT (F0589) 03.559 UT (F0590), days 88 and 89, using the G111 and G227 grisms with the instrument configured using a long-slit ($4''7 \times 191''$), yielding a spectral resolving power $R = \lambda/\Delta\lambda \sim 140\text{--}300$. the G111 grating was used to observe V1047 Cen both nights. Standard pipeline processed and flux calibrated data (for details of the reduction processes see Clarke et al. 2015) were retrieved for science analysis from the Infrared Processing and Analysis Center (IPAC) Infrared Science Archives (IRSA). The data products contain a computed atmospheric transmission model appropriate for the flight altitudes which were used to mask-out spectral points in the observed spectral energy distributions where the atmospheric transmission was $\lesssim 70\%$. Within the statistical errors, no variations between the G111 data sets obtained on the two different nights were noted, hence these data were averaged into a single resultant spectrum.

2.4. MeerKAT observations

We observed the field of V1047 Cen with the MeerKAT radio interferometer (Jonas & MeerKAT Team 2016) 15 times between days 277 and 700. Observations were taken with the 64 antenna array at a central frequency of 1.28 GHz with a 856 MHz bandwidth. Each

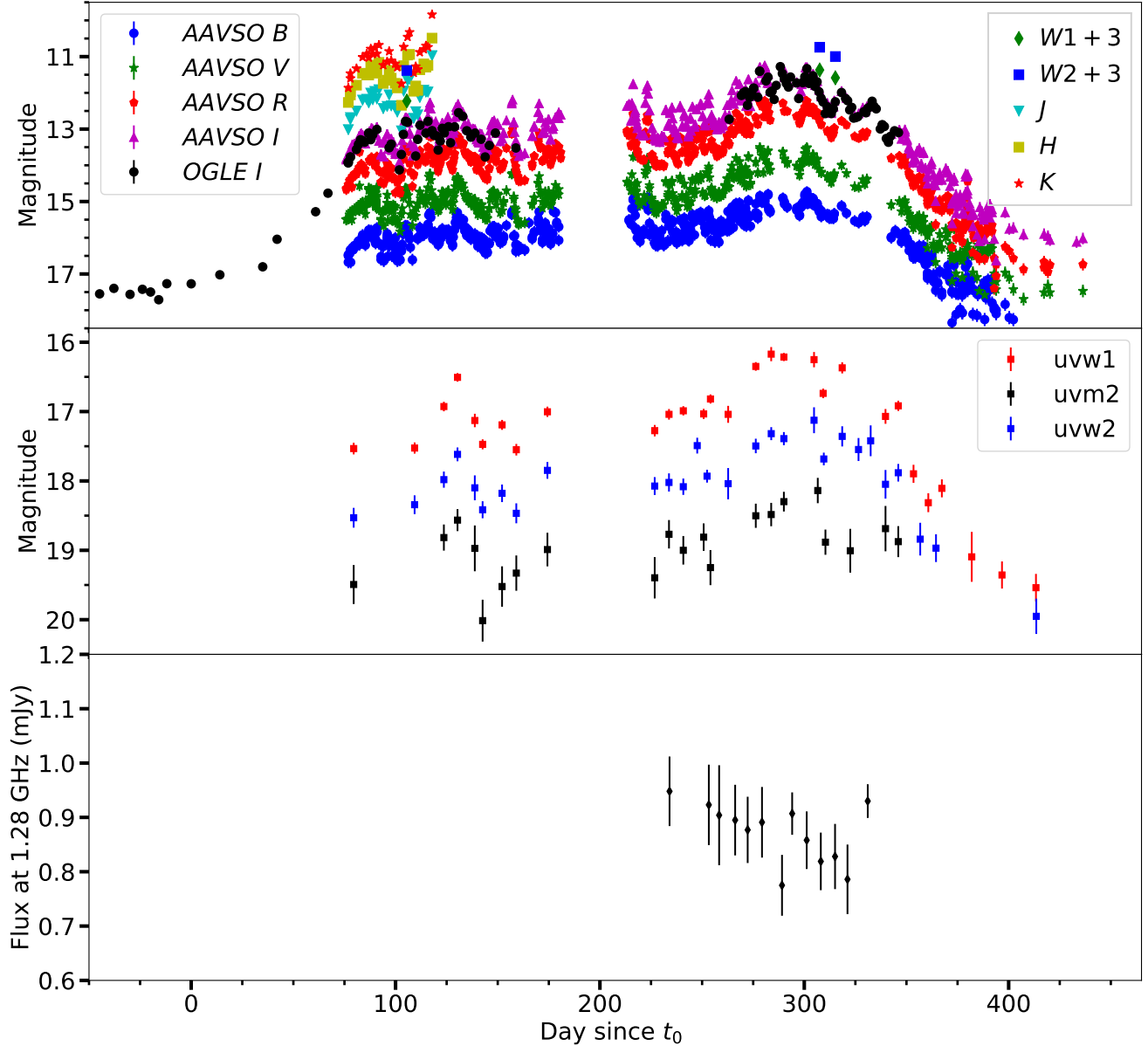


Figure 2. Multi-band light curves of the 2019 outburst of V1047 Cen. The *top panel* shows optical and IR photometry from AAVSO (*BVRI*), OGLE (*I*), SMARTS (*JHK*), and NEOWISE (*W1* and *W2*) photometry. The *middle panel* shows *Swift* UVOT UV data, and the *bottom panel* shows MeerKAT L-band radio flux at 1.28 GHz. Colors and symbols are coded as indicated in figure legends.

observation consisted of 15 minutes integration on the field of V1047 Cen with two minutes on the phase calibrator J1424–4913 before and after. J1939–6342 was used to set the flux scale and calibrate the bandpass response of the instrument. Data were reduced using the OxKAT (see Heywood 2020 for details) reduction scripts, which include recipes for both phase reference and amplitude and phase self-calibration. The typical noise in a region of our images without obvious emission

is $35 \mu\text{Jy}/\text{beam}$. A log of the MeerKAT observations is given in Table A.7

2.5. *Swift* observations

Observations of V1047 Cen with *Swift* commenced on 2019 June 24, 79 days after the re-brightening start. The UV/Optical Telescope (UVOT; Burrows et al. 2005; Roming et al. 2005) detected emission across all three UV filters (*uvw1*: central wavelength of 2600 \AA ; *uvm2*:

2246 Å; $uvw2$: 1928 Å; a sample of the observations is listed in Table A.8). No X-ray emission was detected with the X-ray Telescope (XRT), however. A second observation was performed a month later (day 109), followed by approximately weekly observations from day 123 until day 420 after the start of the outburst. Throughout this time, a variable UV source was detected, while no individual observations showed significant X-ray emission. Co-adding the full ~ 50 ks of XRT data, a faint X-ray source with a count rate of $2.8^{+1.3}_{-1.1} \times 10^{-4}$ count s^{-1} was detected. However, with only 16 counts in the source extraction region, no spectral analysis can be sensibly performed.

3. RESULTS

3.1. Optical/UV light curves

The AAVSO ($BVRI$), OGLE I , and *Swift* UV light curves of V1047 Cen are presented in Figure 2. The data reveal peculiar behavior, with the outburst lasting for around 400 days. There is a general trend of increased brightness between days 0 and ~ 310 , before the brightness of the system starts decreasing. Throughout the 400 day outburst, the light curves show variability of the order of a few days and with amplitude variations of $\lesssim 1$ magnitude. Based on the OGLE data the amplitude of the outburst exceeded 6 magnitudes (Figure 1).

The evolution of the optical broadband colors $(B - V)_0$, $(V - R)_0$, and $(R - I)_0$ is presented in Figure 3. We applied a reddening correction based on the $E(B - V)$ extinction derived in Section 4.1. The colors show random fluctuations around a mean value throughout the majority of the outburst. However, on day 250, the three colors show a noticeable redward trend, coincident with a bump in the optical light curves. This is followed by a blueward trend after day 300, as the outburst ends.

We have near-IR photometry only for a short period near the start of the plateau. Aside from a trend toward redder colors as the source brightened (between days 76 and 82, corresponding to late part of the rising phase), the near-IR colors were fairly stable, at $I - K = 2.25 \pm 0.03$, $J - K = 1.24 \pm 0.02$, and $H - K = 0.51 \pm 0.03$.

Using the optical and UV photometry, we created spectral energy distributions (SEDs) during different stages of the outburst (the rise – from start to day 90; the plateau – between days 90 and 300; and the decline – after day 300; Figure 4). We fit blackbody functions to the SEDs to estimate the temperature of the emitting source. The best-fit blackbody models fit the data poorly, indicating complex emission, possibly from multiple sources (e.g, the nebula of the 2005 nova event, the white dwarf surface, the accretion disk, and ejected material/outflow). Therefore, caution is required when

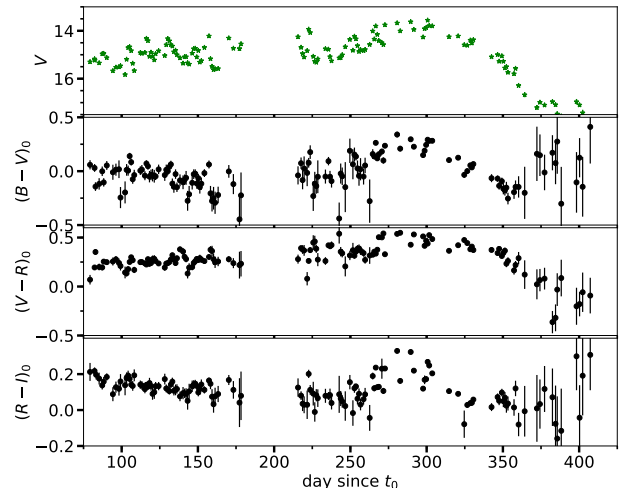


Figure 3. The evolution of the extinction-corrected broadband colors $(B - V)_0$, $(V - R)_0$, and $(R - I)_0$, throughout the outburst.

interpreting a blackbody fit. That being said, throughout the outburst, the temperatures derived from the best fit blackbody models are in the range of 17000 K to 21000 K. These are somewhat high compared to the temperatures modeled for DN outbursts in the outer part of the disk (~ 10000 K Godon et al. 2020) but is in the right range for the temperatures in the inner part of the disk (between 30000 and 60000 K Long 1996; Godon et al. 2017). In GK Per outburst, Kim et al. (1992) estimated an accretion disk temperature of around 6000 to 10000 K in the outer part of the disk based on their disk-instability-induced outburst model. The $(B - V)_0$ colors of V1047 Cen range between -0.3 and $+0.3$, with an average value of ≈ 0.0 throughout the outburst (Figure 3), which translates to a blackbody temperature between 7000 K and 16000 K, with an average blackbody temperature of around 10000 K. These temperatures are consistent with those expected in a disk instability event. We do not have simultaneous $BVRIJHK$ and UV data, but in one single instance (day ≈ 308), we have simultaneous optical, UV, and NEOWISE NIR photometry. We create the SED from these observations and we present the best fit blackbody model, which shows a similar outcome to the above conclusions (Figure A.1). However, what is most important about this SED is that it shows how poorly the blackbody model fits the data, implying that any blackbody temperatures derived from the SEDs or even color indices are not reliable.

3.2. Timing analysis of the optical light curves

The *TESS* light curve of V1047 Cen, presented in Figure 5, shows the early rise of the outburst between days

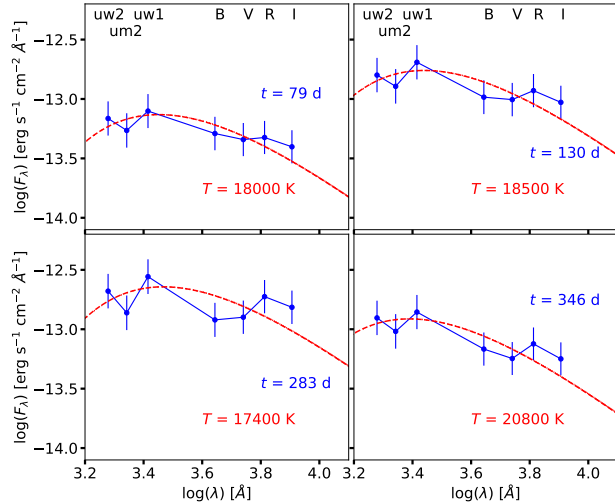


Figure 4. Extinction-corrected SED plots, showing the evolution of the SED throughout different phases of the outburst. The error bars are 1σ uncertainties and they include contributions from the photometric and extinction uncertainties. The red-dashed curves represent the best fit blackbody models. The days of the observations are indicated in blue. The temperatures quoted are derived from the best fit blackbody model.

17 and 44. We searched for periodicity in the *TESS* data by computing the Lomb-Scargle periodogram (Lomb 1976; Scargle 1982; VanderPlas 2018) after detrending the light curve. The periodogram shows modulation at a period of $P_{TESS} = 0.361 \pm 0.030$ days (Figure 5). The period uncertainty is conservatively estimated as

$$P_{\text{error}} = P^2/(2T), \quad (1)$$

values

corresponding to a period change that would cause the easily noticeable phase shift of 0.5 between the first and the last points in the light curve. The *TESS* light curve covers the time range of $T = 21.5$ days after detrending and removing the outlier measurements. The peak-to-peak amplitude of the periodic variations is about 0.04 mag in the *TESS* photometric band (Figure A.2).

To confirm the significance of the detected periodicity, we compute the false alarm probability of 10^{-4} using eq. (14) of Scargle (1982) and estimating the number of independent frequencies (208 for the trial period range 0.1–3 days) following the prescription in sec. 5.3 of Schwarzenberg-Czerny (2003). We confirm the above false alarm probability estimate with 10^4 iterations of bootstrapping (e.g., sec. 7.4.2.3. of VanderPlas 2018). The periodic signal persists whether we use polynomial or piecewise linear detrending techniques. The signal can also be recovered from different subsections of the

TESS light curve and is not associated with any known instrumental period signal.

We also performed Lomb-Scargle periodogram analysis of the photometric data collected by the AAVSO observers in *B*, *V*, *R*, *I* and *CV* (clear filter observations with *V* zero-point) bands. In the section of the light curve between $t_0 + 76$ days (when the multi-color photometric observations start) and the seasonal gap starting on $t_0 + 181$ days, we found a period of $P_{AAVSO} = 8.36 \pm 0.33$ days. The period is derived from a light curve combining measurements in all filters, its uncertainty is estimated using Eq. (1). The Lomb-Scargle false alarm probability is $> 10^{-5}$ for each photometric band and much lower for the combined light curve. The amplitude of the periodic variations is ~ 1.2 mag in *V* band (Figure A.2). With the low false alarm probability, detection in different photometric bands as well as the subsets of data collected by individual observers (Josch Hamsch, Godron Meyer) and 12 cycles covered before the seasonal gap, the detection of P_{AAVSO} can be regarded as highly significant.

Surprisingly, P_{AAVSO} completely disappears from the AAVSO light curve after the seasonal gap.

P_{AAVSO} is not found in the *TESS* data, however detrending removes variations on the relevant timescales. The duration of the *TESS* light curve is only $3.2 \times P_{AAVSO}$, so periodic variations on this timescale cannot be properly probed with these data.

While the *TESS* data set spans only 27.5 days, the AAVSO broadband data span several hundred days and some nights include time-resolved photometry. Therefore, one should expect to find the period P_{TESS} in the AAVSO data; however it was not found. The variations with period P_{TESS} could have been missed due to a combination of their low amplitude and difficulties in detrending (large night-to-night variations while the duration of each night's run is $< P_{TESS}$).

Due to the large difference between P_{TESS} and P_{AAVSO} , it is very unlikely that one of them is the orbital period while the other is the superhump period (see e.g., Patterson et al. 2005; Pearson 2006; Smith et al. 2007; Smak 2020 and references therein). While based on the Stolz & Schoembs (1984) relation, the orbital period-superhump period excess and the orbital period are correlated, for an orbital period of 0.361 days, the superhump period should be around 15 hours (Otulakowska-Hypka et al. 2016). Based on the current data, it is not possible to confirm whether one of these periods is the orbital or superhump period. However, there is other evidence that suggests the longer 8.36 d period is indeed the orbital period of the bi-

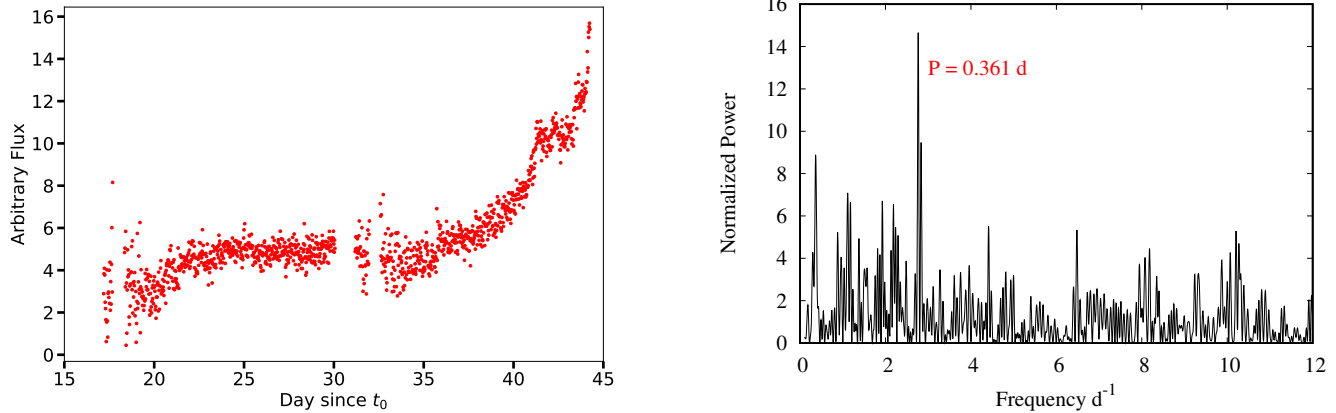


Figure 5. *Left:* the *TESS* light curve of the 2019 outburst of V1047 Cen. *Right:* Lomb-Scargle Periodogram of the *TESS* data showing modulation at a period of 0.361 ± 0.03 days.

nary, implying an evolved secondary (see Section 4 for additional discussion).

It is possible that the two transient periods may be associated with different structures within the binary system. The structure associated with the eruption and responsible for P_{AAVSO} (perhaps the expanded atmosphere of the accreting white dwarf) may outshine the structure responsible for P_{TESS} (perhaps the accretion disk) that was dominating the light of the system in quiescence and at the initial stages of the brightness rise. This could lead to the *TESS* variations becoming swamped and hence undetectable, even if present in the underlying system.

After the seasonal gap, the *AAVSO* lightcurve reveals irregular variations on a timescale of days with amplitudes reaching 1 mag. The switch from nearly-periodic (with P_{AAVSO}) to irregular variations could reflect a change in physical conditions of the emitting region, such as pulsation from the expanded atmosphere of the white dwarf (e.g., Schenker 2002). Another possibility for the disappearance of the P_{AAVSO} after the seasonal gap is that the inner part of the binary system is hidden by an optically thick outflow that started around day 230 after outburst (see Section 4.5).

3.3. Radio light curve and spectral indices

The MeerKAT radio light curve is plotted in Figure 2. The *L*-band (900 - 1670 MHz) flux shows variability between $\simeq 0.7$ and 1.0 mJy during the optical outburst. There is no obvious correlation between the optical and radio emission. At day 700, ten months after the end of the optical outburst, the radio emission from the system is still bright at $\simeq 0.91$ mJy (Figure 7).

We derived the spectral indices of the MeerKAT observations on days 258, 301, and 421 (Figure 7). To do

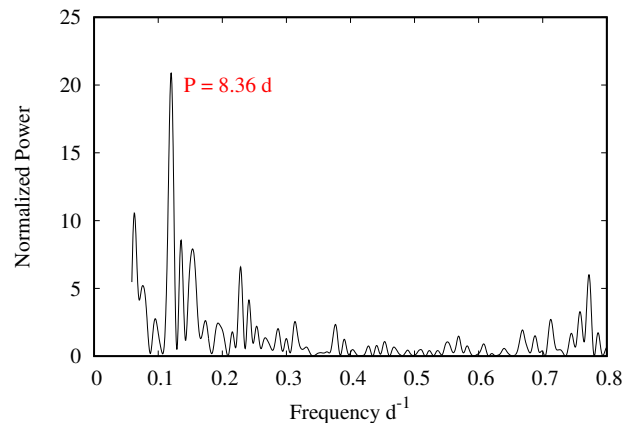


Figure 6. Lomb-Scargle Periodogram of the *V*-band data showing modulation at a period of 8.36 ± 0.33 days.

that, we divided the data into eight frequency intervals centered at 859 MHz, 1.016 GHz, 1.123 GHz, 1.230 GHz, 1.337 GHz, 1.444 GHz, 1.551 GHz, and 1.658 GHz, allowing us to measure the flux density of the source at each sub-band. Consequently we calculated the spectral index, α , by fitting a single power law to the radio spectra that is represented as: $S \propto \nu^\alpha$. We note that the sub-band calibration for MeerKAT is still an active area of exploration, and hence the systematic uncertainties on the sub-band flux densities may yet be underestimated. While the spectrum is mostly flat, given the large uncertainties in the spectral indices, caution is required when interpreting these indices. Overall, it is hard to draw strong conclusions from these values, other than that the radio emission is not optically thick. We elaborate more on the origin of the radio emission in Section 4.

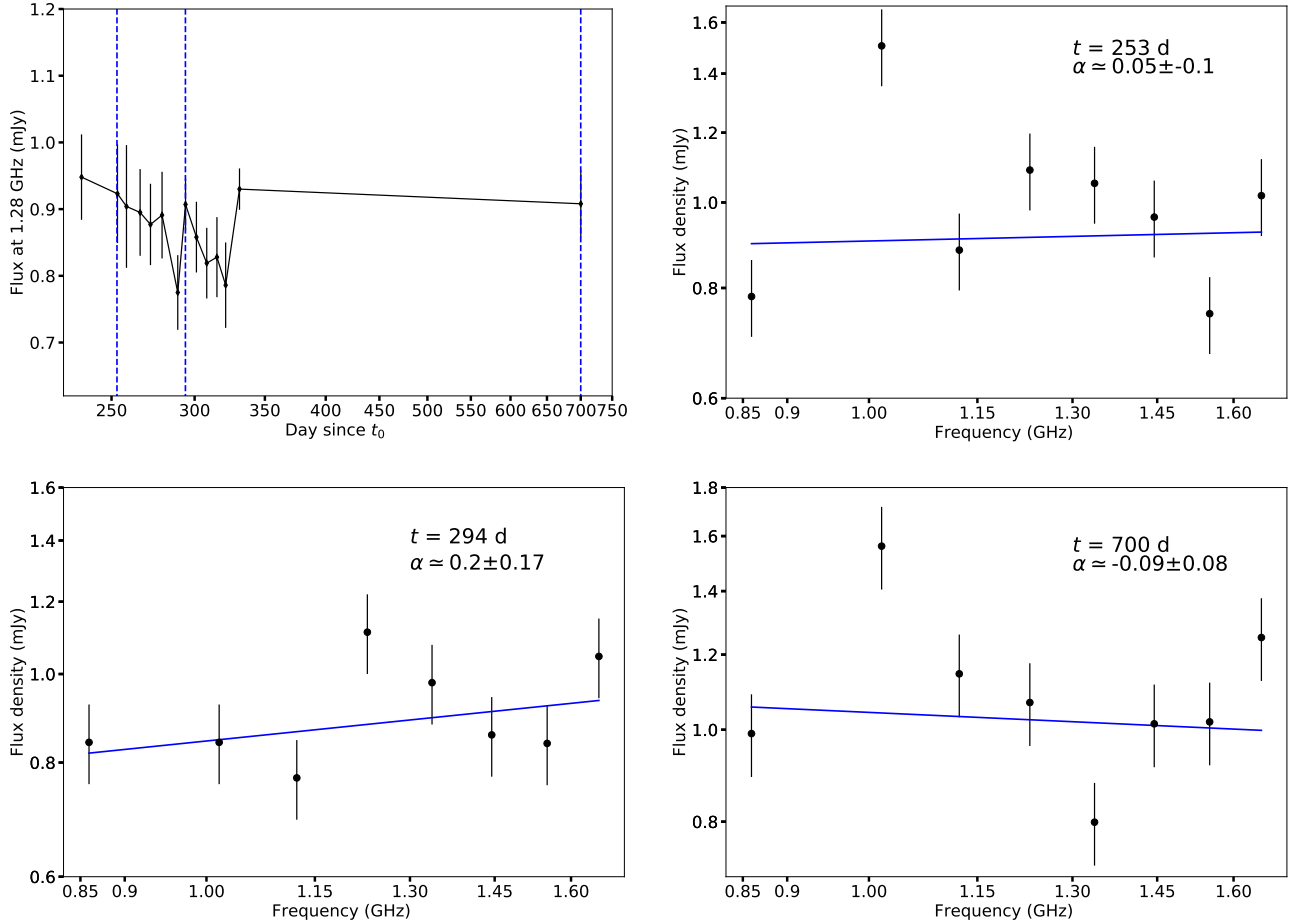


Figure 7. The MeerKAT radio light curve measured at 1.28 GHz is plotted in the *top left panel*, for comparison with three radio spectra measured on days 256, 294, and 700. Spectral indices are listed in each panel. The vertical dashed lines on the light curve plot signify the epochs when spectra are measured.

3.4. Optical spectral evolution

In Figure 8 we present a sample of the optical spectra, evolving throughout the outburst of V1047 Cen and covering three stages: the rise (day 74), the plateau phase (days 113 and 303), and the post-outburst (day 407). The full spectral evolution is presented in Figures A.3 to A.7. The first spectrum, obtained 74 days after the start of the outburst, shows relatively narrow emission lines of H (Balmer) and He I, with Full Widths at Half Maximum (FWHMs) $< 300 \text{ km s}^{-1}$ and Full Widths at Zero intensity (FWZIs) of around 500 km s^{-1} , which are typical features of a DN outburst (e.g., Morales-Rueda & Marsh 2002). These features co-exist and are superimposed on top of broader emission lines of H, [O III], and C VI, with FWZIs of around 2500 km s^{-1} for the Balmer lines and 1100 km s^{-1} for the [O III] lines, which are characteristic of a classical nova nebula (likely arising in the remnant of the 2005 nova eruption). We also identify an even narrower feature in the Balmer lines, during the

first 2 spectral epochs (days 74 and 81), characterized by FWHMs of $< 40 \text{ km s}^{-1}$ (see Figures 9 and A.10). While we do not have a definite explanation for the origin of these narrow features, it might be originating in a dense circumbinary medium related to the presence of an evolved secondary (see Section 4.2).

By day 113, the fluxes of the Balmer lines had increased significantly relative to the [O III] lines $F_{H\alpha}/F_{5007} = 1.56$ on day 74, compared with ~ 15 on day 113 and (e.g., $F_{H\beta}/F_{5007}$ increased from ~ 0.35 on day 74 to ~ 3.1 on day 113; see Figure 10 for a direct comparison between the evolution of $H\beta$ and the [O III] lines). The high-resolution spectra show that the Balmer and [O III] line profiles are very different from one another, with the [O III] lines (in the high-resolution spectra) having rectangular shapes and jagged tops, characteristic of nova nebular lines. In contrast, $H\beta$ shows complex profiles which vary throughout the outburst. The Balmer lines also had significantly broadened, with the FWZIs

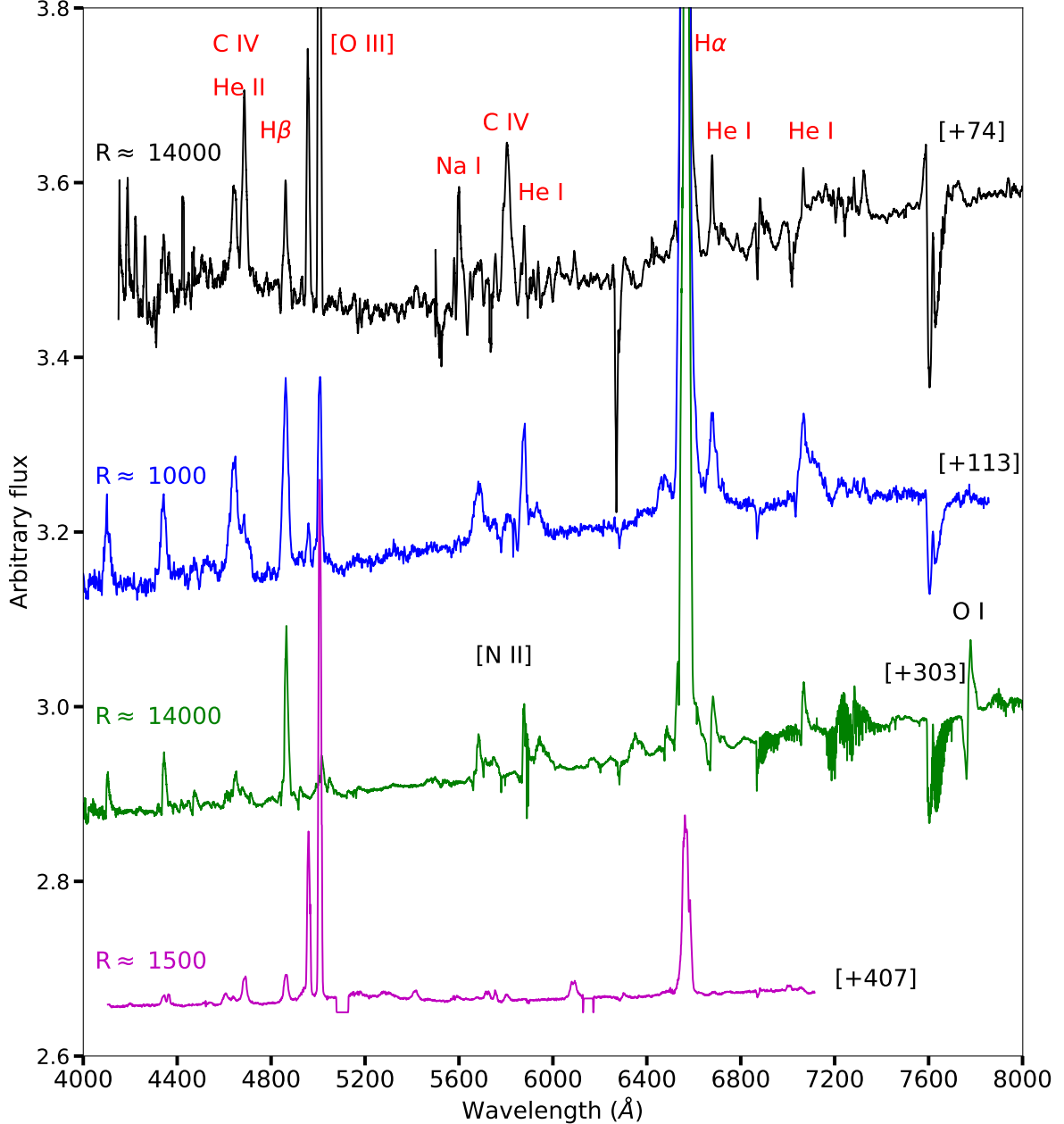


Figure 8. The optical spectral evolution of V1047 Cen throughout different stages of its outburst. The numbers in brackets are days since t_0 . We also quote the resolving power of the spectra on the plot. Note that the calibration pipeline introduced artifacts in the continuum of the spectrum of day 74, particularly below 5000 Å.

increasing by factors of ~ 2 compared to day 74, reaching $4000\text{--}4500\text{ km s}^{-1}$ (Figures 9 and 10). Note that a broad base in $H\alpha$ can be observed as early as day 81 but it becomes prominent from day 113 onwards.

From day 130, some of the He I emission lines show P Cygni profiles with absorption troughs at blueshifted velocities of around 1400 km s^{-1} (Figures A.4 and A.5).

Between days 262 and 303 O I and N II emission lines emerge, while the [O III] nebular lines fade relative to the other spectral lines. At this stage, in addition to the He I emission lines, Balmer, N II and O I emission lines also show P Cygni profiles with absorption troughs at velocities of around -1200 to -1400 km s^{-1} (Figure 11). During the same period, particularly on days 281 and 286, the optical spectra which extend above

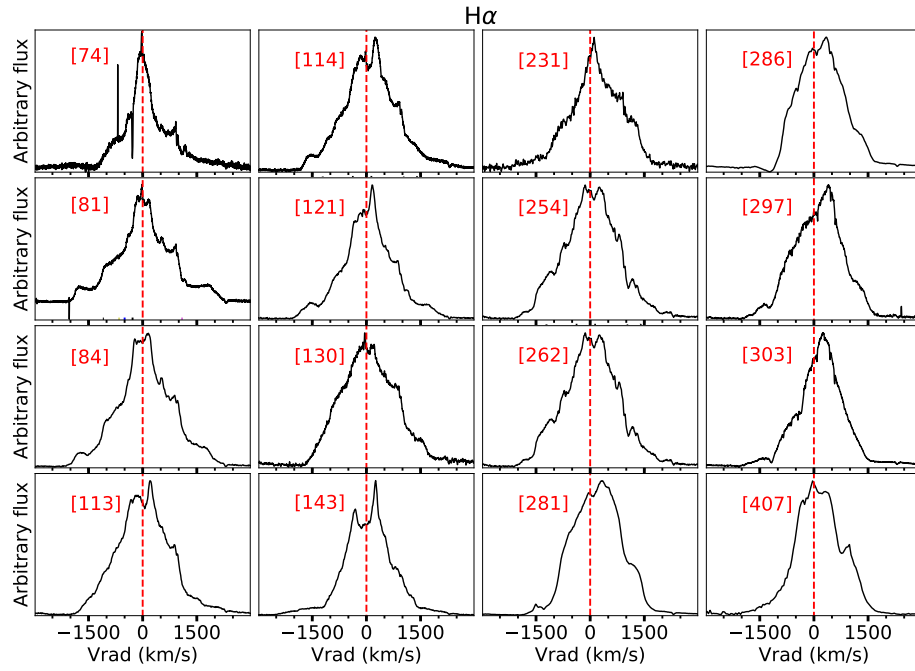


Figure 9. The line profile evolution of $H\alpha$ throughout the outburst of V1047 Cen. The numbers between brackets are days after outburst. The red dashed lines represents the rest velocity ($V_{\text{vrad}} = 0 \text{ km s}^{-1}$). A heliocentric correction is applied to the radial velocities.

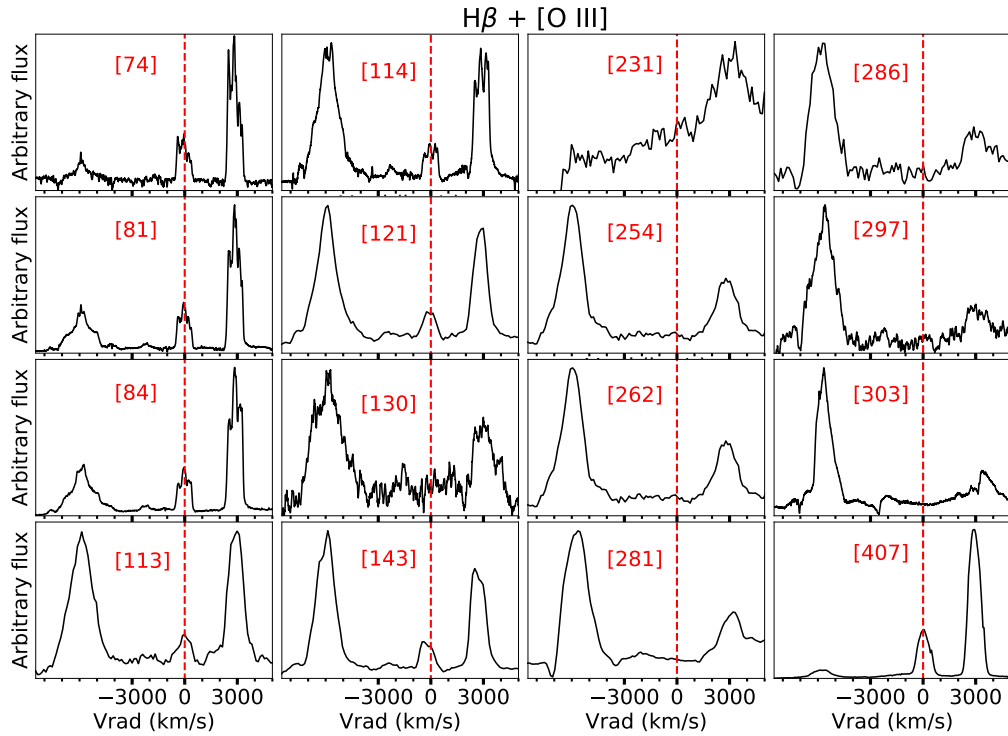


Figure 10. The evolution of the profiles of the $[O \text{ III}]$ lines at 4959 and 5007 Å in comparison to $H\beta$, throughout the outburst of V1047 Cen. The numbers between brackets are days after outburst. The red dashed lines represents the rest velocity ($V_{\text{vrad}} = 0 \text{ km s}^{-1}$) of $[O \text{ III}]$ 4959 Å. A heliocentric correction is applied to the radial velocities.

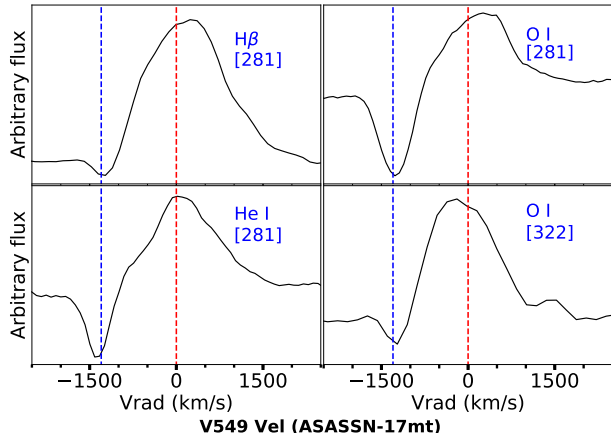


Figure 11. The P Cygni line profiles of H β , He I 7065 Å, and O I 7773 Å taken on day 281 and O I 1.128 μm taken on day 322 (Numbers between brackets are days since t_0). The red and blue dashed lines represent $v_r = 0 \text{ km}^{-1}$ and $v_r = -1300 \text{ km}^{-1}$, respectively.

8000 Å show broad double-peaked emission of O I at 8446 Å with FWZIs of around 3600 km s^{-1} (Figure A.9). The O I P Cygni profile at 7773 Å and the double-peaked O I 8446 Å are not typical features of DN outbursts (Morales-Rueda & Marsh 2002).

After the end of the optical outburst, the spectrum obtained on day 407 shows substantial changes (Figure 8), with the [O III] emission lines now dominating the spectrum relative to the Balmer lines. In Figure 12 we show the evolution of the line ratio between the [O III] line at 5007 Å and H β and the evolution of the equivalent width of H β , [O III] 5007 Å, and [O III] 4995 Å emission lines. It is remarkable how the [O III] lines were still relatively strong during the rise of the 2019 outburst, but fade throughout the outburst, before strengthening again relative to the Balmer lines by the end of the outburst.

Half a year later, our spectra on days 615 and 643 still show strong [O III] lines, in addition to other lines, which likely originate in the 2005 classical nova nebula, such as [O II] 7320 Å, [N II] 5755 Å, and high ionization [Fe VII] lines (Figure A.7).

Our last spectrum taken on day 774, more than 2 years after the start of the 2019 outburst, shows in addition to the 2005 nova nebular lines, weak lines from high ionization transitions of He, N, O, and C, such as the He II lines at 4686 and 5412 Å, N V 4603 Å, O V 5920 Å, C IV 5802 Å, and O IV 7713 Å or Ne IV 7716 Å (Figure A.8). Such lines have been observed in systems like V617 Sgr and V Sge and are associated with nuclear shell burning (e.g., Herbig et al. 1965; Cieslinski et al. 1999; Steiner et al. 1999).

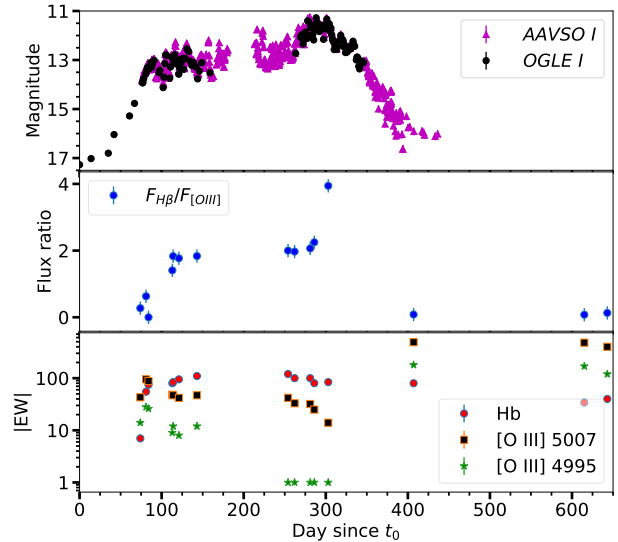


Figure 12. *Top:* the optical light curve in the I -band. *Middle:* The evolution of the flux ratio between H β and [O III] 5007 Å. *Bottom:* The evolution of the equivalent width (EW) of the H β , [O III] 5007 Å, and [O III] 4995 Å emission lines.

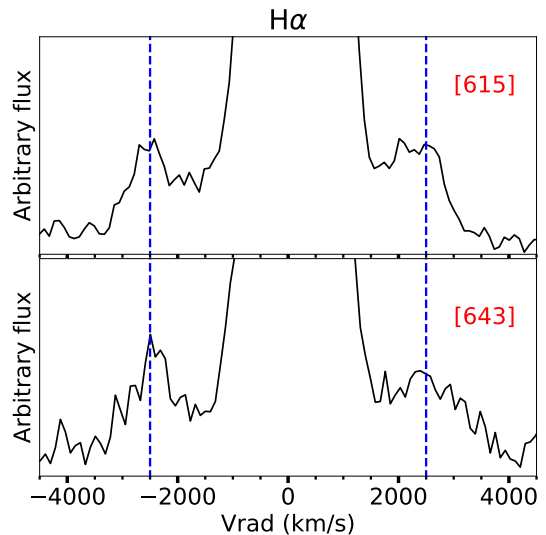


Figure 13. High-velocity “satellite” features in the late H α line profiles, taken on days 615 and 643. The origin of these features is considered in the Discussion.

Several months after the end of the optical outburst on days 615 and 643, H α shows satellite emission components at $\pm 2500 \text{ km s}^{-1}$ (Figures 13 and A.7). We elaborate on the origin of these components in the discussion.

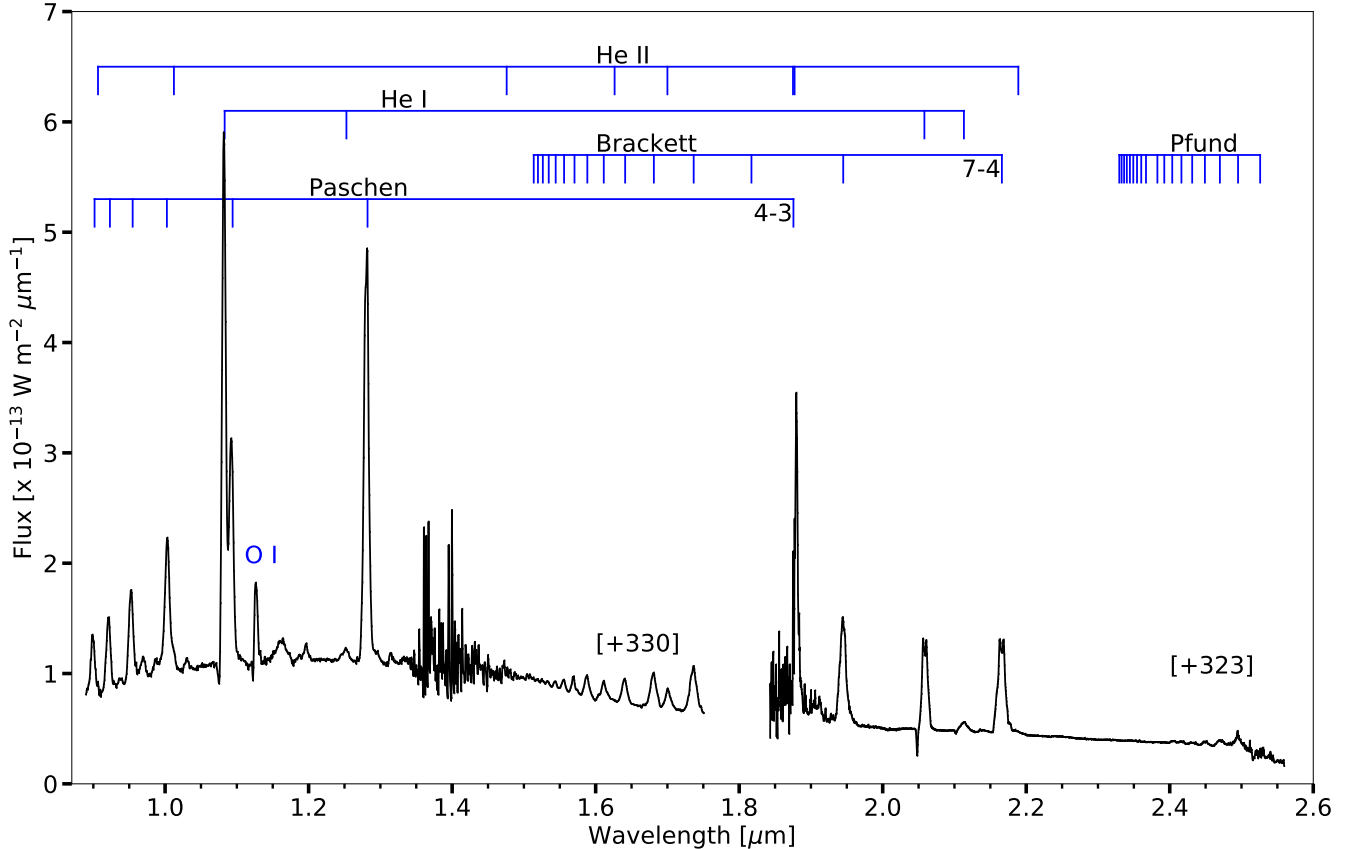


Figure 14. The Gemini-S 0.9–2.5 μm spectra obtained on days 323 and 330. We identify hydrogen recombination and other He and O lines. For the recombination lines, we show the transition of the longest wavelength member.

3.5. IR spectral evolution

The Gemini and SOFIA IR spectra are represented in Figures 14 and 15, respectively. A detailed description and analysis of the IR spectral evolution during the first 120 days of the outburst is presented in Geballe et al. (2019). The Gemini *JHK* spectra obtained on day 322 show emission lines of H I (Paschen, Brackett, and Pfund series), He I, He II, and O I. The FWZIs of the lines are around 4000 km s^{-1} , similar to the ones measured from the optical spectral lines. The O I line at $1.1289 \mu\text{m}$ and some of the H I and He I lines show P Cygni profiles with absorption troughs at blue-shifted velocities of 1100 to 1800 km s^{-1} , also comparable to the ones measured for optical lines (Figure 11).

Figure 15 presents the SOFIA composite spectra obtained on day 87, including contemporaneous, dereddened (see § 4.1) *BVRI* photometry obtained from the AAVSO database, as well as NEOWISE photometry obtained 18 days later. A blackbody fit to the 2019 SOFIA spectra yields $T_{\text{bb}} = 425 \pm 12 \text{ K}$, which we interpret as thermal emission from circumstellar material

heated by the outburst event. WISE photometry obtained in 2010 (prior to the eruption) is also plotted and a blackbody fit to this photometry yields a cooler temperature of $T_{\text{bb}} = 315 \pm 30 \text{ K}$. Thus the circumstellar material (dust, likely from the 2005 nova event) has been heated as a result of processes related to the 2019 outburst. The SOFIA spectra show no evidence for strong H or He I emission lines on day 87. However the [O IV] $25.91 \mu\text{m}$ fine structure line, frequently seen in other novae (Gehrz et al. 2015; Evans & Gehrz 2012; Helton et al. 2012) is marginally detected. A Gaussian fit gives a line flux of $6.9 \pm 1.6 \text{ W m}^{-2}$. The upper level of this line is collisionally de-excited at electron densities (n_e) in excess of $9.9 \times 10^3 \text{ cm}^{-3}$ (for an electron temperatures of 10^4 K); the presence of the line therefore indicates that the electron density in the region where the line is produced is less than this value.

3.6. The 2005 eruption vs the 2019 outburst

The 2005 nova eruption, reached magnitudes brighter than 8 mag in the visual, compared to a peak *V*-band magnitude of 13.5 for the 2019 outburst (Figure 1 and 2).

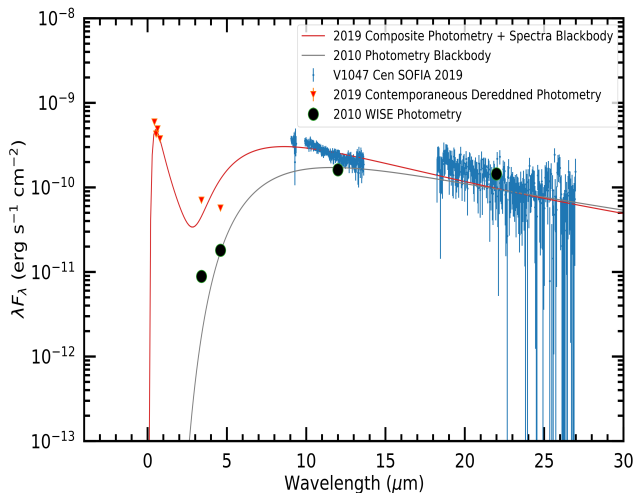


Figure 15. The 2019 SOFIA mid-infrared spectra of V1047 Cen obtained on day 87. The blue symbols are the SOFIA spectra (combination of two grating settings G111 and G227) which includes all spectral points where the atmospheric transmission at the flight altitudes are great than 70% (hence the gap near $\sim 9.5 \mu\text{m}$). The wavelength coverage of the two gratings is not continuous. Superposed is the best-fit composite blackbody (red solid line), i.e., the sum of a $T_{\text{bb}} = 7070 \pm 950 \text{ K}$ from the 2019 photometry data plus a $T_{\text{bb}} = 425 \pm 12 \text{ K}$, the latter is interpreted as thermal emission from heated circumstellar material (dust) from the blast of the 2019 eruption. The inverted orange triangles are contemporaneous (2019) dereddened $BVRI$ and NEOWISE photometry, while the filled-black circles are 2010 WISE photometry showing that the infrared spectral energy distribution peak was represented by a cooler blackbody (solid gray line) of $T_{\text{bb}} = 315 \pm 30 \text{ K}$.

These translate to an absolute visual magnitude of ≈ -8 for the 2005 eruption and ≈ -2 for the 2019 outburst, using $A_V = 3.03$ and a distance of 3.2 kpc (see Section 4.1). This clearly implies that the 2005 event was much more energetic than the 2019 one. The morphology of the optical light curves are also distinctively different with the 2005 light curve typical of a fast nova, while the light curve of the 2019 event plateaued for around a year. The velocities measured from the spectra taken during the 2005 eruption range from 750 to 1800 km s^{-1} . These velocities are slow to moderate in comparison to the velocities observed in classical novae. During the rise of the 2019 outburst, the velocities measured from some of the lines were around a few hundreds km s^{-1} (typical of CVs), but later in the outburst, the spectral lines showed velocities of $\lesssim 2000 \text{ km s}^{-1}$, raising questions about the nature of this event.

4. DISCUSSION

4.1. Reddening and distance

In order to derive the reddening towards the system, we use the equivalent widths of several absorption lines from diffuse interstellar bands, in combination with the empirical relations from Friedman et al. (2011). We derive an average $E(B-V) \approx 1.0 \pm 0.1$ and $A_V = 3.0 \pm 0.1$ for $R_V = 3.1$, in good agreement with the results of Geballe et al. (2019). We avoid using the interstellar Na I D absorption doublet due to saturation.

The Gaia parallax measurement of V1047 Cen suffers from large uncertainties. The latest Gaia EDR3 parallax of the system is $0.338 \pm 0.249 \text{ mas}$ (Gaia Collaboration et al. 2021). With a flat prior (Galactic latitude-based priors are not appropriate for novae), this implies a distance of $2.7^{+3.9}_{-1.0} \text{ kpc}$, which is not a useful constraint.

Due to the high uncertainty in the Gaia parallax, we use the three dimensional Galactic reddening maps from Chen et al. (2019) and our measured reddening value to estimate the distance to V1047 Cen. The reddening map uses measurements from the Gaia DR2, 2MASS and WISE surveys. Therefore, we converted the previously derived $E(B-V)$ measurement to reddening values in the 2MASS JHK filters and the Gaia DR2 G , G_{Bp} , and G_{Rp} bands, using the extinction law from Wang & Chen (2019) and Chen et al. (2019). We derive $E(G-K_s) = 2.2 \pm 0.1$, $E(G_{Bp}-G_{Rp}) = 1.3 \pm 0.1$, and $E(H-K_s) = 0.2 \pm 0.1$. Using these reddening values, we derive an average distance of $3.2 \pm 0.2 \text{ kpc}$, consistent with the Gaia parallax distance within its large uncertainties. The above uncertainty for the reddening-based distance likely underestimates the systematic uncertainties in this calculation.

4.2. Evolutionary stage of the secondary

If the 8.36 day period found in the AAVSO data is the orbital period of the system, given that the donor is filling its Roche lobe, it implies that the star is evolved, either a subgiant or a lower luminosity red giant (Webbink et al. 1983). Two similar examples are (1) V392 Per (Nova Per 2018), which has an orbital period of 3.51 days, and has been demonstrated by Munari et al. (2020) to host a subgiant secondary; and (2) GK Per, which has an orbital period of 1.9 days and hosts a subgiant K secondary star (Bianchini et al. 1981). The 8.36 days period would be the longest for a CV that showed a nova eruption, but is on the shorter end for systems with luminous red giant secondaries, which are typically characterized by periods of the order of hundreds of days (Whitelock 1987; Mikołajewska 2003). This would make V1047 Cen an intermediate system between typical CVs and systems with luminous giant secondaries (symbiotic

systems; Kenyon 1986; Mikolajewska et al. 1988; Munari 2019).

The average V - and I -band magnitudes as measured by OGLE long after the nova, between 2013 and 2018, are $I = 17.12$ and $V = 17.5$. The post-nova color index is then $(V - I) = 0.38 \pm 0.07$, implying $(V - I)_0 = -1.19$. In Figure 16 we show the OGLE light curve during the six years prior to the 2019 outburst. Adopting a distance of 3.2 kpc and $A_I = 1.46$, we derive $M_I \approx 3.5$ during the post-nova period. While this value is consistent with the absolute magnitude of a subgiant star, we also expect contributions from the accretion disk, hot spot, and the 2005 nova nebula. Therefore, using the optical magnitudes/colors during quiescence to constrain the evolutionary stage of the companion star is not straightforward. We note that the system is not listed in the USNO-B1.0 catalog (Monet et al. 2003), and is not apparent in visual inspection of blue or red plates of the Digitized Sky Survey (DSS; Figure 16). Since the completeness level of this survey is roughly $V \sim 20.5$ – 21 mag, this suggests the quiescent magnitude of the system is fainter than in the post-nova OGLE imaging and rules out anything more luminous than a marginally evolved secondary. In Figure 16, we show charts of the field of V1047 Cen from DSS (red plates taken in Feb. 1999), OGLE (taken in Feb 2014), and SOAR (taken in June 2019). Clearly, there is an excess in brightness of the system in 2014, nine years after the 2005 nova eruption, compared to pre-nova. This indicates that the system did not return to the pre-nova brightness, which could be due to ongoing nuclear burning on the surface of the white dwarf.

The OGLE $(V - I)$ colors between 2010 and 2019 indicate a blue source with extremely high temperatures, in excess of 10^5 K. These nonphysically blue colors (for an evolved or main sequence star) could be due to the contribution of emission lines to the spectra. Particularly, the forbidden O III lines from the nova nebula, whose fluxes contribute to the V -band. These lines were relatively strong compared to the other lines during the early spectra of the 2019 outburst and after the end of the outburst (Figure 8). Unlike the V -band, no strong nebular lines contribute to the flux in the I -band (Figure A.3). In addition, the blue colors could again indicate that ongoing nuclear burning on the surface of the WD. Some nova systems have shown continued thermonuclear burning on the surface of the WD several years after nova eruptions (e.g., Zemko et al. 2015, 2016), but these authors' conclusions rely mostly on delayed X-ray emission. In systems where the nuclear burning lasts for several years after nova erup-

tions, the masses of the WDs are expected to be low ($M_{\text{WD}} < 1 M_{\odot}$; Wolf et al. 2013; Henze et al. 2014).

Note that the *Swift* non-detection of V1047 Cen on April 2008, less than 3 years after the 2005 nova, argues against residual nuclear burning on the white dwarf. If residual nuclear burning is ongoing on the white dwarf we expect to detect supersoft X-ray emission (e.g., Page et al. 2020) from the system, unless the nova ejecta were still optically thick to the supersoft emission from the white dwarf 3 years after the nova. Alternatively, nuclear burning could have resumed on the white dwarf at a low rate, a few years after the nova, due to enhanced mass-transfer rate from an irradiated, evolved companion.

4.3. The 2019 outburst of V1047 Cen - a record breaker

Only a few classical novae are known to have shown DN outbursts after a nova eruption, such as GK Per (Nova Persei 1901; Sabbadin & Bianchini 1983; Bianchini et al. 1986), V1017 Sgr (Nova Sagittarii 1919; Sekiguchi 1992; Salazar et al. 2017) and V446 Her (Nova Herculis 1960; Honeycutt et al. 1995, 2011). The first DN outbursts of these novae were recorded 47 years (GK Per), 54 years (V1017 Sgr), and 30 years (V446 Her) after the nova eruption. The 14 year gap between the classical nova eruption and the 2019 outburst of V1047 Cen is the shortest ever recorded, if it is indeed a DN outburst. Note that the older novae such as GK Per and V1017 Sgr might have had earlier DN outbursts that were missed due to monitoring gaps.

The rise to peak of V1047 Cen, its plateau phase, and its decline lasted 100, 210, and 100 days, respectively. This 400 day outburst is twice as long as the longest known DN outburst, previously recorded for V1017 Sgr and four times longer than the longest outburst recorded for GK Per (e.g., the 2006 outburst; Evans et al. 2009).

The peak absolute magnitude at V -band during the 2019 outburst reached ≈ -2 mag. This is higher than the typical absolute magnitude of dwarf novae during outburst, which ranges between 3.8 and 2.6 (Ramsay et al. 2017). Some systems with long periods (of the order of days) such as V1017 Sgr and V630 Cas, have more than usual luminous DN outbursts, with absolute magnitudes reaching -0.3 and 1.4 , respectively. However, even these are still substantially less luminous compared to V1047 Cen. Therefore, if 2019 outburst of V1047 Cen is a DN, it would be the most luminous outburst of a DN observed to date. Note that Kawash et al. (2021) showed that some DN outbursts could reach absolute magnitudes brighter than zero but accurate distances

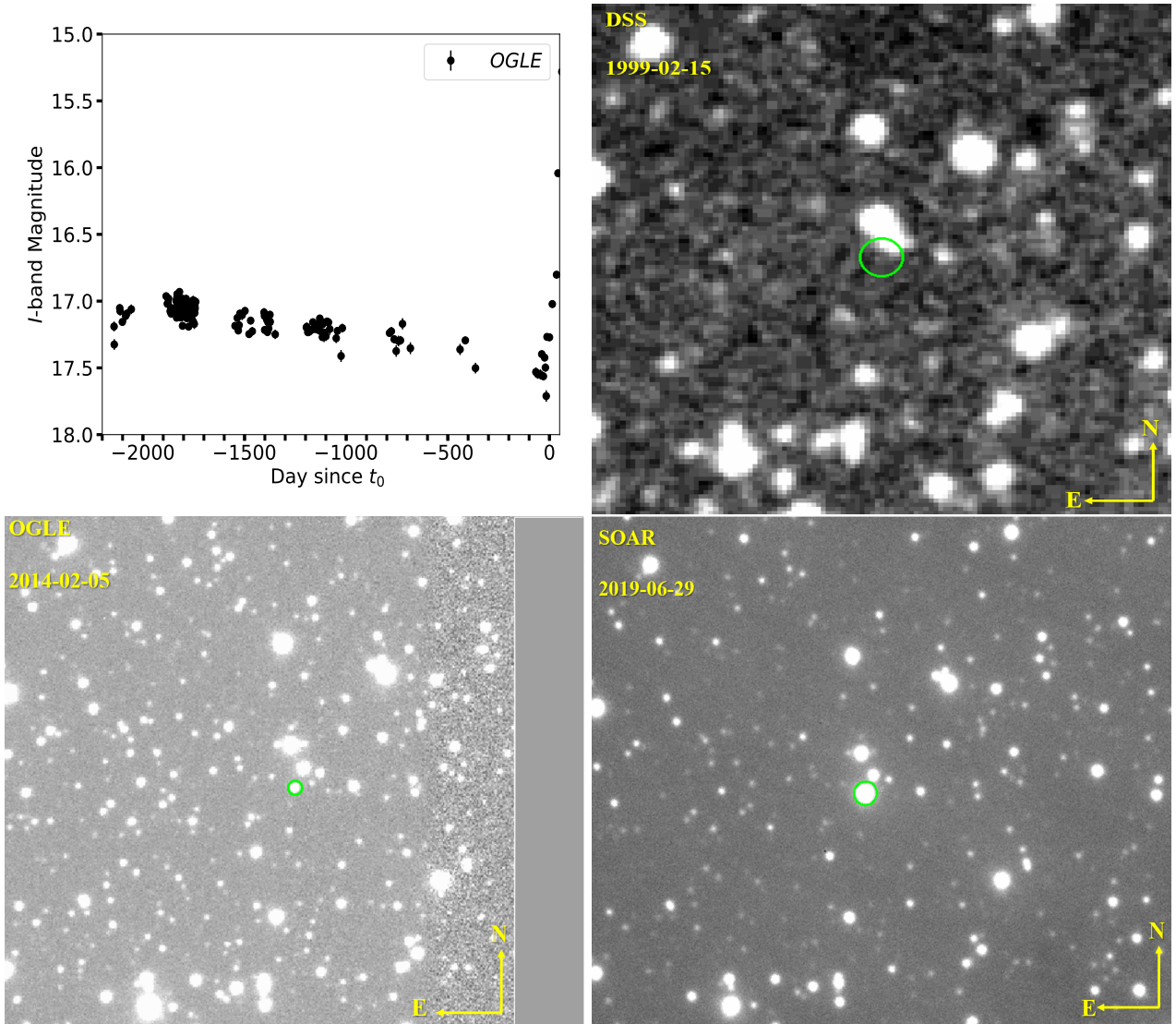


Figure 16. *Top-left:* the OGLE light curve between 2013 and 2019. Days are relative to the 2019 outburst start. *Top-right:* A red plate of the field of V1047 Cen from the Digitized Sky Survey (DSS) obtained in February 1999 (position of V1047 Cen indicated by a green circle). *Bottom-left:* combined OGLE images of V1047 Cen (circled in green) taken between in February 2014. *Bottom-right:* SOAR acquisition image of V1047 Cen (circled in green) taken during the in June 2019, during the 2019 outburst. In all the charts the field is 2×2 arcmin. V1047 Cen lies on the edge of the OGLE images, which is the reason why the chart is cropped on the west edge.

and extinction values were unavailable for these systems in Kawash et al.’s study.

DNe are known to show a diversity of light curve morphologies, even in one system. These outbursts could be narrow (a rise and decline with only a short period of time spent at peak/plateau), or wide and long (characterized by an extended plateau phase; Hellier 2001).

The narrow but slow outbursts of V1017 Sgr show a short plateau of less than three weeks (Salazar et al. 2017), in contrast to the very long (more than 200 days) plateau duration of V1047 Cen. However, the morphology of the light curve of V1047 Cen is more similar

to some of the outbursts of GK Per, particularly the 2006 one, which lasted for around 100 days and showed substantial variability during a plateau interval of more than 2 months (Evans et al. 2009). The plateau phase of a DN occurs when the entire accretion disk enters outburst and sustains it, with matter continuously falling onto the white dwarf. In some cases, enhanced mass transfer due to irradiation of the companion star helps sustain the plateau for an extended period of time (Hellier 2001).

The decline rate of DN outbursts is known to correlate with the orbital period of the system. This rela-

tion is known as the Bailey relation (Bailey 1975), and is particularly valid for systems above the period gap (Otulakowska-Hypka et al. 2016). The rise rate is associated with the direction of the propagation of the heating or instability wave, whether it is propagating outside-in (rapid rise) or inside-out (slow rise; see Otulakowska-Hypka et al. 2016 and references therein). But the rise time should also be correlated with the size of the disk and therefore, the orbital period of the system (Warner 2003). If the 2019 V1047 Cen is a DN outburst, the slow rise rate indicates an outburst propagating inside-out in a system with an orbital period of the order of a few days. We used a rise rate of $\approx 25 \text{ d mag}^{-1}$ measured from the *OGLE* light curve, and the empirical relations of both Warner (2003) and Otulakowska-Hypka et al. (2016), to estimate an orbital period of ≈ 3.8 days and 29.1 days, respectively. While the relations suffer from large uncertainties, they both indicate that the system should have an orbital period of the order of days up to a few weeks. We also used similar relations from both of the above papers which relate the rate of decline to the orbital period. Using these relations and a decline rate of 28.75 d mag^{-1} , we derive periods of ≈ 4.9 days and 2.9 days, from the relations of Warner (2003) and Otulakowska-Hypka et al. (2016), respectively.

Both Smak (2000) and Otulakowska-Hypka et al. (2016) also found a correlation between the orbital period and duration of the outburst. Based on this relation and an outburst duration of 400 days, the orbital period of the system is also expected to be of the order of days. Note that the duration of the outburst of V1047 Cen is an outlier to the sample used in these studies. While all these relations suffer from large uncertainties, they all indicate that the system is very likely to have an orbital period of the order of days, which is consistent with the 8.36 days period found in the AAVSO data.

4.4. Implications for the hibernation scenario

The hibernation scenario, which was first suggested to explain the apparent lack of nova eruptions in CV systems showing DNe, suggests that all CVs undergo cycles of low and high states of mass transfer rate (Shara et al. 1986). After a classical nova eruption, the hibernation scenario predicts that the CV undergoes a phase of high-mass transfer rate due to irradiation of the secondary by the hot white dwarf; this can last for several centuries (Hillman et al. 2020). However, due to mass loss in the nova eruption, the binary now has a wider separation, and as irradiation shuts off and the secondary relaxes into its new Roche lobe, the mass transfer rate will drop and perhaps even turn off entirely. During this hibernation phase, standard angular momentum loss mecha-

nisms like magnetic braking will act, gradually bringing the binary into contact again. Mass transfer will then resume onto the white dwarf surface, eventually accumulating enough accreted material to trigger the next classical nova eruption.

During the state of high mass transfer after a classical nova eruption ($\dot{M} \approx 10^{-8} M_{\odot} \text{ yr}^{-1}$), the system is not expected to undergo DN outbursts, which require lower mass transfer rates of the order of $\sim 10^{-10} M_{\odot} \text{ yr}^{-1}$ (Osaki 1974; Cannizzo et al. 1988; Warner 1995). Therefore, the 14 year gap between the 2005 nova eruption and 2019 outburst of V1047 Cen challenges the hibernation scenario on one hand and raises question about the nature of this outburst on the other hand.

However, for systems with orbital periods of a few days, DN outbursts could still take place a few decades after a nova eruption, during a phase of high mass transfer. This is because, in systems characterized by long orbital periods, the accretion disk is large enough that the critical mass accretion rate, below which DN outbursts are possible, is also large. This critical mass accretion rate scales with the radius of the accretion disk as $R^{2.6}$ (Kim et al. 1992; Cannizzo 1993; Warner 1995; Geballe et al. 2019). Therefore, in the cases of GK Per and V1017 Sgr, with orbital periods around 2 and 5.7 days respectively, the fact that they show DN outbursts soon after nova eruptions is not surprising (Kim et al. 1992). If the period of 8.36 days found in the broadband AAVSO photometry is the orbital period of V1047 Cen, its accretion disk—and the critical mass transfer rate below which outbursts are possible—is even larger than in GK Per and V1017 Sgr.

If the period of 0.361 days derived from the *TESS* data is the orbital period of the system, then the size of V1047 Cen’s accretion disk is still within the typical range for CVs. In this case it is more challenging to explain the 14 year gap between the nova eruption and the 2019 outburst. However, V446 Her, which was observed to show regular DN outbursts three decades after its classical nova eruption in 1960, is characterized by a period of 0.207 days (Honeycutt et al. 1995, 2011). This could mean that under certain conditions, a DN outburst is still possible during post-nova high mass transfer rate conditions, even if the system is harboring an average size accretion disk. It is therefore essential to accurately constrain the period of the system spectroscopically, which will be the aim of future work.

4.5. Origin of the spectral features

During the rise phase (days 0 to 90), the spectrum of V1047 Cen resembled that of a DN superimposed on a spectrum of an old classical nova shell. However, the

subsequent evolution, particularly of the Balmer lines, differed considerably from that of DNe. The widths of the Balmer lines reached velocities much larger than those of the nova's nebular lines, with FWZIs of around 4000 km s^{-1} (compared to FWZIs $\approx 1100 \text{ km s}^{-1}$ for the latter). These velocities are also much larger than those measured for the Balmer lines during GK Per's recent outburst (FWHM $\sim 500\text{-}650 \text{ km s}^{-1}$; e.g., Wilber et al. 2015). The Balmer lines also showed substantial increases in their line fluxes relative to the nova nebular lines more than 100 days into the 2019 outburst (Figure 10). The cause of this dramatic flux increase and broadening is not clear, but it could be due to a fast, low density outflow. All this indicates that, in addition to the potential DN outburst, there are other mechanisms shaping the electromagnetic signatures of V1047 Cen.

Between days 262 and 310, most of the lines in the spectrum (e.g., Balmer, He I, and O I) showed P Cygni-like absorption features at velocities of around -1400 km s^{-1} . Such features are not characteristic of a DN outburst. They probably originate in an optically thick wind/outflow. The onset of these features coincides with the start of the brightness increase between days ≈ 260 and 310 (Figure 2), supporting the possibility of a wind or shell ejection during this phase of the outburst.

The satellite emission components at $\pm 2500 \text{ km s}^{-1}$ in H α around 7 months after the end of the outburst, are reminiscent of the features observed in Z And-like classical symbiotic outbursts. They are associated with collimated bipolar flows (see e.g., Burmeister & Leedj arv 2007; Skopal et al. 2013; Tomov & Tomova 2013).

4.6. The origin of the bright radio emission

In the past decade, CVs have been established as radio emitters during both quiescent and outburst phases (e.g., C ordova et al. 1983; Coppejans et al. 2015, 2016; Barrett et al. 2017). Their radio properties are diverse, and the emission mechanisms powering CV radio luminosity are still being established.

Coppejans et al. (2015) observed several nova-like CVs and found that they are significant radio emitters. Nova-like CVs are non-magnetic CVs characterized by a sufficiently high mass transfer rate to maintain the accretion disk in a constant hot state, unlike CV systems which undergo DN outbursts. For the individual systems in their sample, Coppejans et al. (2015) found that the emission in these nova-like CVs is consistent with optically thick synchrotron, gyro-synchrotron, or cyclotron maser emission. Their 6 GHz spectral radio luminosities are $\sim 10^{15} - 10^{17} \text{ erg s}^{-1} \text{ Hz}^{-1}$ (Coppejans et al. 2015).

Non-magnetic CVs which undergo DN outbursts are also known to be radio sources during outburst (Coppejans et al. 2016). The most famous of these systems is SS Cyg, which shows a radio flare during the early days of its optical outbursts, peaking at $\sim 1 \text{ mJy}$ before fading gradually, dropping below radio detectability by the end of the optical outburst. This flaring radio emission resembles that of X-ray binaries (XRBs) and is suggested to be the result of synchrotron emission from a transient jet (e.g., K ording et al. 2008; Miller-Jones et al. 2011; Russell et al. 2016; Coppejans et al. 2016; Coppejans & Knigge 2020). Coppejans et al. (2016) found that the specific radio luminosities of DNe in outburst range between 10^{14} and $10^{16} \text{ erg s}^{-1} \text{ Hz}^{-1}$ at 10 GHz.

Based on a radio survey targeting a large sample of magnetic CVs, Barrett et al. (2017) suggest that they are also radio emitters, dominated by weakly polarized gyrosynchrotron emission or highly polarized electron-cyclotron maser emission. Most of these are nearby (less than a kpc) sources and are characterized by flux densities, $\sim 20\text{-}400 \mu\text{Jy}$; the implication is radio spectral luminosities in the range $\sim 10^{14} - 10^{17} \text{ erg s}^{-1} \text{ Hz}^{-1}$ (Barrett et al. 2020). Only one of them, AE Aqr, shows substantially higher flux density ($\sim 5 \text{ mJy}$), but it is located remarkably nearby, at a distance of $\approx 90 \text{ pc}$ (Ramsay et al. 2017).

Similar to the other observational features of V1047 Cen across the spectrum, the radio emission from this system is record breaking and puzzling. Assuming a distance of 3.2 kpc, the spectral luminosity of V1047 Cen at 2 GHz is $\sim 10^{19} \text{ erg s}^{-1} \text{ Hz}^{-1}$. This means that V1047 Cen is at least two orders of magnitude brighter at radio wavelengths than other cataclysmic variables.

If the radio emission from a DN outburst is optically thick thermal emission from ionized gas at a typical brightness temperature of $10^4 - 10^5 \text{ K}$, the emitting regions should have radii of $\sim 10^{14} - 10^{15} \text{ cm}$ (assuming circular sources as projected on the sky) to produce the observed flux densities in V1047 Cen. During a DN outburst, it is reasonable to assume that the emitting gas has a size equal to the size of the binary. CVs with orbital periods of the order of a few hours have orbital radii of $\sim 10^{11} \text{ cm}$. Even for CVs with orbital periods of around 9 days, the orbital radius is $\sim 10^{12} \text{ cm}$, still at least two orders of magnitude smaller in size than the optically thick emitting gas responsible for the observed fluxes. This implies that if the outburst is a DN, any emission of order the size of the orbit must be non-thermal (brightness temperature $> 10^5 \text{ K}$).

One possibility is that the radio emission is non-thermal synchrotron emission from a transient radio jet, similar to the case of other DN outbursts. While the flux

density of V1047 Cen equals that of SS Cyg during its short-lasting flare, the luminosity of V1047 Cen is several orders of magnitude brighter than that of SS Cyg (the distance to SS Cyg is ≈ 114 pc). In Figure 17 we plot V1047 Cen on the L_{radio} vs L_X diagram in comparison with jet emission in other CVs and other astrophysical events such as XRBs, accreting millisecond X-ray pulsars, and transitional millisecond pulsars (we multiply the spectral luminosity by 5 GHz to estimate the radio luminosity at 5 GHz assuming a flat spectrum). V1047 Cen’s 5 GHz luminosity, $\sim 1 \times 10^{29}$ erg s $^{-1}$, is much higher than that observed in CVs and is comparable to (or even brighter in some cases than) XRBs and pulsars with compact primaries like neutron stars and black holes. Such an energetic jet should also be a bright X-ray source. We used WebPIMMS³ to derive the X-ray unabsorbed flux using the stacked *Swift* X-ray detection and assuming a 5 keV thermal bremsstrahlung model and $N(H) = 8.4 \times 10^{21}$ cm $^{-2}$ (we use $N(H) = 2.81 \times 10^{21}$ A_V ; Bahramian et al. 2015). This translates to an X-ray luminosity of around 3.7×10^{31} erg s $^{-1}$ at a distance of 3.2 kpc, which is comparable to the X-ray luminosity of other CVs in outburst.

It is not possible to determine if V1047 Cen showed flaring radio emission during the early days of the outburst like SS Cyg and was an even brighter radio source at that time, or if the ~ 1 mJy emission remained more or less constant throughout the optical outburst. Nevertheless, what is really puzzling is that at the end of the optical outburst, the radio flux did not drop. This is in contrast to the trends shown by SS Cyg and other DN outbursts, where the radio flux drops below the detection limit by the end of the optical outburst (Russell et al. 2016). This disparity between the radio behavior and energetics of V1047 Cen and other DN outbursts raises additional questions about the origin of the radio emission in V1047 Cen and if a transient synchrotron jet is an appropriate explanation.

Bode et al. (1987) conducted a radio survey of 26 classical novae observed with the VLA less than 10 years after eruption and detected only two in the sample. Both novae were detected at 5 GHz, 2 years (V4077 Sgr) and 8 years (NQ Vul) after the nova eruptions. The emission from these two novae was suggested to be thermal and had radio spectral luminosities $\sim 10^{18} - 10^{19}$ erg s $^{-1}$ Hz $^{-1}$. The higher-end radio spectral luminosity of V4077 Sgr is due to the fact that the system was observed only 2 years after the nova eruption; radio emission from classical novae often peaks on timescales $\sim 1-3$

yr after eruption (Chomiuk et al. 2021). In addition, given that radio emission from decade old or older nova ejecta originates in the nova’s extended thermal remnant, it can vary only slowly, not on the weeks–months timescales observed in V1047 Cen (Chomiuk et al. 2021). Therefore, it is very unlikely that the radio emission from V1047 Cen originates in the ejecta of the 2005 classical nova eruption.

The long-lasting, luminous radio emission in V1047 Cen is remarkably similar to the radio emission from Z And-like classical symbiotic, accretion-powered, outbursts (e.g., Crocker et al. 2001; Mikołajewska 2002; Brocksopp et al. 2004; Sokoloski et al. 2006). These systems are luminous radio sources ($L \approx 10^{18} - 10^{19}$ erg s $^{-1}$ Hz $^{-1}$; Ogley et al. 2002; Brocksopp et al. 2004), where the emission is usually suggested to be thermal, originating from bipolar collimated jets/outflows. Classical symbiotic systems consist of giant stars, which in most cases do not fill their Roche Lobes, transferring material onto WDs; accretion can proceed via a disk or not, depending on the relative velocity of the red giant wind and the accreting WD (Livio 1992; Mohamed & Podsiadlowski 2007). Even out of outburst, symbiotic stars can be luminous radio emitters ($L \approx 10^{17} - 10^{20}$ erg s $^{-1}$ Hz $^{-1}$), as the hot accreting white dwarf ionizes the substantial circumstellar material expelled by the giant companion (Seaquist et al. 1984; Seaquist & Taylor 1990).

We showed earlier that if the radio emission is optically thick thermal emission from an ionized gas at a typical brightness temperature of $10^4 - 10^5$ K, the emitting regions should have a radius of $\sim 10^{14} - 10^{15}$ cm to produce the observed flux densities. If the radio emission observed from V1047 Cen proves to be transient and associated with the 2019 outburst, it might be attributed to outflows moving at velocities $\gtrsim 2000$ km s $^{-1}$ (based on the optical line profiles), which will cover a radius of more than 10^{15} cm in less than 2 months. The variability of the radio source can then be explained as variability in the fast outflow. If V1047 Cen remains a luminous radio source out of outburst, the radio emission may instead be attributable to circumstellar material, expelled by the potentially evolved companion (assuming an 8.36 day orbital period) and ionized by the hot WD.

4.7. The nature of the outburst

The spectroscopic follow up of V1047 Cen, during the rise to peak (first 90 days) is fairly consistent with a DN spectrum; however, the 400 day long outburst, the 14 year gap between the 2005 nova eruption and the 2019 outburst, the luminous radio and optical emission, the dramatic spectral changes and high velocity spectral

³ <https://heasarc.gsfc.nasa.gov/cgi-bin/Tools/w3pimms/w3pimms.pl>

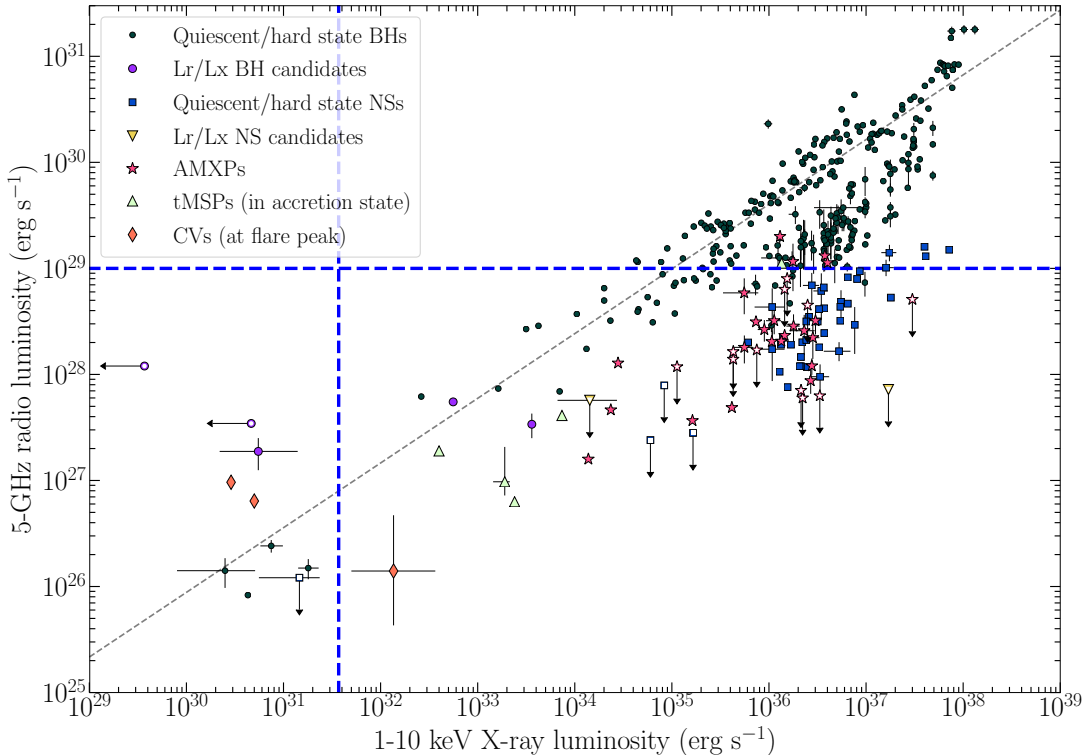


Figure 17. The plane of 5 GHz radio luminosity (L_{radio}) vs. 1–10 keV X-ray luminosity (L_X), with points representing X-ray binaries (accreting neutron stars, black holes), accreting and transitional millisecond pulsars, and CVs. The radio luminosity of V1047 Cen at 5 GHz is plotted with dashed blue horizontal line and is calculated assuming a flat spectrum. Adopted from Bahramian et al. (2018) <https://zenodo.org/record/1252036/export/hx>.

components all raise questions about the nature of this event.

If the 0.361 day period found in the *TESS* data is the orbital period of the system, it would be challenging to explain the observational features of the system as a DN outburst. However, if the 8.36 day period found in the AAVSO data is the orbital period, the system could potentially host a large accretion disk (maybe one of the largest in currently known CV systems), which has the potential to explain some of the record-breaking observational features, such as the short gap between the nova eruption and DN outburst and the 400 day outburst. This could potentially place V1047 Cen along with GK Per and V1017 Sgr in a new class of CVs, which show long-lasting DN outbursts (a few decades after a nova eruption) and are characterized by orbital periods of the order of a few days with mildly evolved secondaries and massive accretion disks. However, some of the observational features of V1047 Cen outburst, such as the long-lasting luminous radio emission and the optical spectral features are challenging to explain in the context of a DN outburst.

Many of the features observed in V1047 Cen resemble those of “combination novae” in Z And-like classi-

cal nova outbursts (Sokoloski et al. 2006). This type of event starts with a disk instability outburst, leading to the accretion of a massive accretion disk onto the white dwarf. The accretion burst is large enough to trigger enhanced nuclear burning on the surface of the white dwarf and the ejection of an optically thick outflow/shell (see also Munari 2019).

While classical symbiotic systems are characterized by orbital periods of the order of hundreds of days (Mikołajewska 2003; much longer than the potential 8.36 days orbital period in V1047 Cen), the observational features of classical symbiotic outbursts have many similarities with those of V1047 Cen (the long-lasting optical outburst, the long-lasting and luminous radio emission, the P Cygni spectral features with velocities $\approx 1500 \text{ km s}^{-1}$, and the satellite spectral features around the Balmer lines).

Therefore, we suggest that the 2019 outburst of V1047 Cen could have indeed started as a DN disk instability type outburst (Based on the early spectroscopy), leading to the accretion of a massive accretion disk onto the white dwarf. The accretion of the large disk might have led to enhanced nuclear shell burning on the surface of the white dwarf, which launched a ra-

radiation driven wind/outflow, as quoted by Sokolowski et al. (2006) “in a milder version of the phenomenon that powers classical novae”. The accretion could have been ongoing for several years at a low level prior to the 2019 outburst (see below). This scenario could explain the 400 day outburst duration in the optical (e.g., the 2000’s outburst of Z And lasted for 2 years) and the dramatic brightening and broadening of the Balmer lines. The light curve bump or re-brightening that occurred ~ 260 days after the outburst start could mark the stage at which an optically thick outflow started. This is consistent with the development of P Cygni-like absorption features in the optical spectral lines around the same period (Figure 11). The absence of the P Cygni profiles in the spectra obtained on day 407 after the end of the optical outburst (Figure 8; note that the P Cygni profiles were present in the previous epoch on day 303) indicates that the optically thick wind/outflow dissipated rapidly and became optically thin, which is very similar to the behavior observed in the combination nova of Z And (Sokolowski et al. 2006). The presence of high ionization lines of He, C, O, and N in the late spectra of V1047 Cen (Figure A.8), obtained after the end of the optical outburst could indicate ongoing nuclear shell burning, which would strengthen the case for a combination nova. The same high ionization lines of N V and O VI are typically observed in V Sge like stars—the Milky-Way counterparts of the supersoft sources in the Magellanic Clouds—typically indicate nuclear shell burning (e.g., Herbig et al. 1965; Cieslinski et al. 1999; Steiner et al. 1999).

The combination nova scenario could also explain the long-lasting, luminous radio emission. We showed in Section 4.6 that the flux densities observed in V1047 Cen could be explained as thermal emission from an outflow of ionized gas. Such radio emitting outflows/jets are characteristics of combination nova events (e.g. Brockopp et al. 2004 and references therein). In addition, there is strong evidence for the presence of such collimated outflows or jets in V1047 Cen based on the satellite emission components observed in $H\alpha$ (Figure 13), which are similar to those observed in Z And-like classical symbiotic outbursts (e.g., Munari et al. 2005; Burmeister & Leedj arv 2007; Skopal et al. 2013; Tomov & Tomova 2013).

If strong internal shocks are not present within the outflow, we do not expect bright X-ray emission, because the X-ray emission associated with the nuclear-burning WD would be hidden by the puffed up photosphere and outflow during the combination nova event. This could explain the lack of X-ray detection in the *Swift* individual observations.

The 8.36 day period is shorter than the typical periods of classical symbiotic systems. Therefore, the V1047 Cen system would be intermediate between typical CVs and classical symbiotics. The latter are also characterized by low mass WDs (Sokolowski et al. 2006). We do not have insight into the mass of the WD in V1047 Cen. The 2005 nova eruption of V1047 Cen did show a rapid decline in the optical light curve, which is indicative of an ejection of a low-mass envelope; low mass ejecta in turn tend to be associated with eruptions occurring on massive WDs (Yaron et al. 2005). However, the ejecta velocities measured from the optical spectral lines during the 2005 classical nova are moderate (Liller et al. 2005), which argues against a massive WD. Hachisu & Kato (2007) derived a WD mass of around $0.7 M_{\odot}$ for V1047 Cen, consistent with a system with a low mass WD. However, the values derived by Hachisu & Kato (2007) are based on poor “eye-fitting” of the visual light curve to their models, and therefore are uncertain.

Sokolowski et al. (2006) suggest that pre-existing quasi-steady shell burning on the WD surface is necessary to trigger a combination nova. Given the scarcity of observations between the 2005 nova eruption and 2019 outburst, it is not possible to definitively know if residual nuclear burning on the surface of the WD has been ongoing after the 2005 eruption. However, OGLE photometry between 2013 and 2019 showed that the system has not returned to the pre-2005-nova brightness and the colors of the system during this period suggest emission from a hot source (see Section 4.2). Both of these indicate that nuclear burning on the WD surface could have been ongoing between 2005 and 2019.

The absence of the system from the DSS images before the 2005 nova eruption, places an upper limit of $V \approx 20.5$ on the system during quiescence. This implies that the absolute magnitude of the system before 2005 is dimmer than 5 mag, leaving a small chance for the companion star to be an evolved sub-giant star, unless both the reddening and distance to the system are not well constrained. This challenges the 8.36 days period and the potential combination nova scenario, and raises more questions about the nature of the outburst.

That being said, a DN outburst seems unlikely to explain all the observational features of the 2019 outburst of V1047 Cen and a phenomenon similar to a combination nova seems to agree better with the observations. If so, this would be the first combination nova observed in a system with an intermediate orbital period between typical CVs and classical symbiotics.

One other possible explanation of the 2019 outburst is that the system experienced a non-ejection nova event.

The extended grid of nova models by Yaron et al. (2005) shows that some combination of parameters might lead to a thermonuclear runaway without ejecting material (see also Fujimoto 1982; Shara et al. 1977). Yaron et al. (2005) suggest that such outbursts cause only a slow increase in luminosity, followed by a slow decay, particularly in the case of low mass WDs where the timescales of the rise and decay could be thousands of days. The supersoft X-ray transient ASASSN-16oh has been suggested to be a thermonuclear runaway event without mass ejection (Hillman et al. 2019). The system showed a slowly rising (1585 days) and declining (268 days) optical light curve, with an amplitude of less than 4 magnitude. While there are similarities between the optical light curves of ASASSN-16oh and V1047 Cen, the former has been detected as a supersoft X-ray source at the distance of the Small Magellanic Cloud. This is very different from the case of V1047 Cen, which was not detected in individual epochs by *Swift* during the 2019 outburst despite our extensive monitoring. In case of a thermonuclear runaway, the luminosity of the supersoft source is expected to be of the order of 10^{38} ergs $^{-1}$, which would have been easily observed at a distance of 3.2 kpc by *Swift*. The supersoft emission of ASASSN-16oh was characterized by a luminosity of around 10^{37} ergs $^{-1}$, which is lower than that expected from the models of non-ejecting thermonuclear runaways. This low luminosity has been attributed to an optically thick accretion disk hiding most of the WD surface. While a massive accretion disk could also be blocking some of the emission from the WD surface in case of V1047 Cen, it is a less likely possibility given the *Swift* non-individual-detections over several months.

5. CONCLUSIONS

We have presented multi-wavelength observations of the 2019 outburst in the 2005 classical nova V1047 Cen. The outburst amplitude reached around 6 magnitudes in the optical and lasted for more than 400 days. We derive a distance of 3.2 ± 0.2 kpc to the system and an peak absolute magnitude of the outburst $M_V = -2$. The first spectra we obtained of the system around 74 days after the start of the outburst were consistent with a disk instability dwarf nova event in a classical nova system. If V1047 Cen is a DN, the event would be a record breaker, making it the longest DN outburst on record, the shortest gap between a nova and DN in a CV system, and the most luminous optical and radio DN outburst. We find a potential orbital period of 8.36 days in the optical photometry, which could explain the long-lasting outburst and the 14 year gap with the nova eruption, however, the observational features of the out-

burst across the electromagnetic spectrum point towards a phenomenon more exotic than just a DN outburst.

We therefore suggest that the event is an outburst resembling those observed in classical symbiotic systems which are known as combination novae. In this scenario, the outburst might have started with a DN-like instability in a massive accretion disk, which then triggered enhanced nuclear shell burning on the surface of the white dwarf and eventually led to an optically thick, radiation driven wind/outflow. This scenario fits well the 400 day outburst duration, the dramatic changes in the optical line profiles and the > 2000 km s $^{-1}$ velocities inferred from these profiles, the P Cygni line profiles which appeared several months after the outburst start, the high peak optical brightness, and most importantly the long-lasting, superluminous radio emission, which likely originates from ionized gas (thermal emission) in collimated bipolar flows, which are characteristic of combination nova events. Strong evidence for such outflows can be seen in the late optical spectral line profiles. Mid-infrared observations also indicate that pre-existing dust — likely formed during the 2005 classical nova eruption — has been heated by the radiation from the 2019 outburst.

Therefore, the 2019 outburst of V1047 Cen could either be a record breaking DN outburst or more likely a combination-nova-like event — a phenomenon observed for the first time in an intermediate system between a CV and a symbiotic system, which has undergone a classical nova eruption.

ACKNOWLEDGMENTS

We thank B. Schaefer for useful discussion. We thank the AAVSO observers from around the world who contributed their magnitude measurements to the AAVSO International Database used in this work.

EA, LC, and KVS acknowledge NSF award AST-1751874, NASA award 11-Fermi 80NSSC18K1746, NASA award 16-Swift 80NSSC21K0173, and a Cottrell fellowship of the Research Corporation. JS was supported by the Packard Foundation. DAHB gratefully acknowledges the receipt of research grants from the National Research Foundation (NRF) of South Africa. PAW kindly acknowledges the National Research Foundation and the University of Cape Town. KLP acknowledges funding from the UK Space Agency. Nova research at Stony Brook University has been made possible by NSF award AST-1611443. MG is supported by the EU Horizon 2020 research and innovation programme under grant agreement No 101004719. A part of this work is based on observations made with the Southern African Large Telescope (SALT), with the

Large Science Programme on transients 2018-2-LSP-001 (PI: DAHB). Polish participation in SALT is funded by grant no. MNiSW DIR/WK/2016/07. This paper was partially based on observations obtained at the Southern Astrophysical Research (SOAR) telescope, which is a joint project of the Ministério da Ciência, Tecnologia e Inovações (MCTI/LNA) do Brasil, the US National Science Foundation's NOIRLab, the University of North Carolina at Chapel Hill (UNC), and Michigan State University (MSU). The OGLE project has received funding from the National Science Centre, Poland, grant MAESTRO 2014/14/A/ST9/00121 to AU. The CHIRON and *Andicam* instruments are managed by the Todd Henry and the SMARTS Consortium. The MeerKAT telescope is operated by the South African Radio Astronomy Observatory, which is a facility of the National Research Foundation, an agency of the Department of Science and Innovation. We acknowledge the use of the ilifu cloud computing facility - www.ilifu.ac.za, a partnership between the University of Cape Town, the University of the Western Cape, the University of Stellenbosch, Sol Plaatje University, the Cape Peninsula University of Technology and the South African Radio Astronomy Observatory. The ilifu facility is supported by contributions from the Inter-University Institute for Data Intensive Astronomy (IDIA - a partnership between the University of Cape Town, the University of Pretoria and the University of the Western Cape), the Computational Biology division at UCT and the Data Intensive Research Initiative of South Africa (DIRISA). This research is based in part on observations obtained at the international Gemini Observatory, a program of NSF's NOIRLab, which is managed by the Association of Universities for Research in Astronomy (AURA) under a cooperative agreement with the National Science Foundation. on behalf of the Gemini Observatory partnership: the National Science Foundation (United States), National Research

Council (Canada), Agencia Nacional de Investigación y Desarrollo (Chile), Ministerio de Ciencia, Tecnología e Innovación (Argentina), Ministério da Ciência, Tecnologia, Inovações e Comunicações (Brazil), and Korea Astronomy and Space Science Institute (Republic of Korea). DPKB is supported by a CSIR Emeritus Scientist grant-in-aid, which is being hosted by the Physical Research Laboratory, Ahmedabad. This work is based in part on observations made with the NASA/DLR Stratospheric Observatory for Infrared Astronomy (SOFIA). SOFIA is jointly operated by the Universities Space Research Association, Inc. (USRA), under NASA contract NNA17BF53C, and the Deutsches SOFIA Institut (DSI) under DLR contract 50 OK 0901 to the University of Stuttgart. Financial support for CEW/RDG related to this work was provided by NASA through award SOF07-0005 issued by USRA to the University of Minnesota. This publication makes use of data products from the Near-Earth Object Wide-field Infrared Survey Explorer (NEOWISE), which is a joint project of the Jet Propulsion Laboratory/California Institute of Technology and the University of Arizona. NEOWISE is funded by the National Aeronautics and Space Administration. VARMR acknowledges financial support from the Fundação para a Ciência e a Tecnologia (FCT) in the form of an exploratory project of reference IF/00498/2015/CP1302/CT0001, and from the Ministério da Ciência, Tecnologia e Ensino Superior (MCTES) through national funds and when applicable co-funded EU funds under the project UIDB/EEA/50008/2020, and supported by Enabling Green E-science for the Square Kilometre Array Research Infrastructure (ENGAGE-SKA), POCI-01-0145-FEDER-022217, and PHOBOS, POCI-01-0145-FEDER029932, funded by Programa Operacional Competitividade e Internacionalização (COMPETE 2020) and FCT, Portugal.

REFERENCES

- 2014, Astronomical Society of the Pacific Conference Series, Vol. 490, *Stella Novae: Past and Future Decades*
- Aydi, E., Buckley, H. D. A., Mroz, P., et al. 2019, *The Astronomer's Telegram*, 12885, 1
- Bahramian, A., Heinke, C. O., Degenaar, N., et al. 2015, *MNRAS*, 452, 3475
- Bahramian, A., Miller-Jones, J., Strader, J., et al. 2018, *Radio/X-ray correlation database for X-ray binaries*, vv0.1, Zenodo, doi:10.5281/zenodo.1252036. <https://doi.org/10.5281/zenodo.1252036>
- Bailey, J. 1975, *Journal of the British Astronomical Association*, 86, 30
- Ballester, P. 1992, in *European Southern Observatory Conference and Workshop Proceedings*, Vol. 41, *European Southern Observatory Conference and Workshop Proceedings*, ed. P. J. Grosbøl & R. C. E. de Ruijsscher, 177
- Barnes, S. I., Cottrell, P. L., Albrow, M. D., et al. 2008, in *Proc. SPIE*, Vol. 7014, *Ground-based and Airborne Instrumentation for Astronomy II*, 70140K

- Barrett, P., Dieck, C., Beasley, A. J., Mason, P. A., & Singh, K. P. 2020, *Advances in Space Research*, 66, 1226
- Barrett, P. E., Dieck, C., Beasley, A. J., Singh, K. P., & Mason, P. A. 2017, *AJ*, 154, 252
- Bianchini, A., Hamzaoglu, E., & Sabbadin, F. 1981, *A&A*, 99, 392
- Bianchini, A., Sabbadin, F., Favero, G. C., & Dalmeri, I. 1986, *A&A*, 160, 367
- Bode, M. F., & Evans, A. 2008, *Classical Novae*
- Bode, M. F., Seaquist, E. R., & Evans, A. 1987, *MNRAS*, 228, 217
- Bramall, D. G., Sharples, R., Tyas, L., et al. 2010, in *Proc. SPIE*, Vol. 7735, *Ground-based and Airborne Instrumentation for Astronomy III*, 77354F
- Bramall, D. G., Schmoll, J., Tyas, L. M. G., et al. 2012, in *Proc. SPIE*, Vol. 8446, *Ground-based and Airborne Instrumentation for Astronomy IV*, 84460A
- Brocksopp, C., Sokoloski, J. L., Kaiser, C., et al. 2004, *MNRAS*, 347, 430
- Buckley, D. A. H., Swart, G. P., & Meiring, J. G. 2006, in *Proc. SPIE*, Vol. 6267, *Society of Photo-Optical Instrumentation Engineers (SPIE) Conference Series*, 62670Z
- Burgh, E. B., Nordsieck, K. H., Kobulnicky, H. A., et al. 2003, in *Society of Photo-Optical Instrumentation Engineers (SPIE) Conference Series*, Vol. 4841, *Instrument Design and Performance for Optical/Infrared Ground-based Telescopes*, ed. M. Iye & A. F. M. Moorwood, 1463–1471
- Burmeister, M., & Leedj arv, L. 2007, *A&A*, 461, L5
- Burrows, D. N., Hill, J. E., Nousek, J. A., et al. 2005, *SSRv*, 120, 165
- Cannizzo, J. K. 1993, *The Limit Cycle Instability in Dwarf Nova Accretion Disks*, 6–40
- Cannizzo, J. K., Shafter, A. W., & Wheeler, J. C. 1988, *ApJ*, 333, 227
- Carey, S. J., Noriega-Crespo, A., Mizuno, D. R., et al. 2009, *PASP*, 121, 76
- Chen, B. Q., Huang, Y., Yuan, H. B., et al. 2019, *MNRAS*, 483, 4277
- Chomiuk, L., Metzger, B. D., & Shen, K. J. 2020, *arXiv e-prints*, arXiv:2011.08751
- Chomiuk, L., Linford, J. D., Aydi, E., et al. 2021, *arXiv e-prints*, arXiv:2107.06251
- Cieslinski, D., Diaz, M. P., & Steiner, J. E. 1999, *AJ*, 117, 534
- Clarke, M., Vacca, W. D., & Shuping, R. Y. 2015, *Astronomical Society of the Pacific Conference Series*, Vol. 495, *Redux: A Common Interface for SOFIA Data Reduction Pipelines*, ed. A. R. Taylor & E. Rosolowsky, 355
- Clemens, J. C., Crain, J. A., & Anderson, R. 2004, in *Proc. SPIE*, Vol. 5492, *Ground-based Instrumentation for Astronomy*, ed. A. F. M. Moorwood & M. Iye, 331–340
- Coppejans, D. L., & Knigge, C. 2020, *NewAR*, 89, 101540
- Coppejans, D. L., K rding, E. G., Miller-Jones, J. C. A., et al. 2015, *MNRAS*, 451, 3801
- , 2016, *MNRAS*, 463, 2229
- C rdova, F. A., Mason, K. O., & Hjellming, R. M. 1983, *PASP*, 95, 69
- Crause, L. A., Sharples, R. M., Bramall, D. G., et al. 2014, in *Proc. SPIE*, Vol. 9147, *Ground-based and Airborne Instrumentation for Astronomy V*, 91476T
- Crawford, S. M., Still, M., Schellart, P., et al. 2010, in *Society of Photo-Optical Instrumentation Engineers (SPIE) Conference Series*, Vol. 7737, *Society of Photo-Optical Instrumentation Engineers (SPIE) Conference Series*, 25
- Crocker, M. M., Davis, R. J., Eyres, S. P. S., et al. 2001, *MNRAS*, 326, 781
- Delgado, A., Harrison, D., Hodgkin, S., et al. 2019, *Transient Name Server Discovery Report*, 2019-985, 1
- Della Valle, M., & Izzo, L. 2020, *A&A Rv*, 28, 3
- Evans, A., & Gehrz, R. D. 2012, *Bulletin of the Astronomical Society of India*, 40, 213
- Evans, P. A., Beardmore, A. P., Osborne, J. P., & Wynn, G. A. 2009, *MNRAS*, 399, 1167
- Feinstein, A. D., Montet, B. T., Foreman-Mackey, D., et al. 2019, *PASP*, 131, 094502
- Friedman, S. D., York, D. G., McCall, B. J., et al. 2011, *ApJ*, 727, 33
- Fujimoto, M. Y. 1982, *ApJ*, 257, 752
- Gaia Collaboration, Brown, A. G. A., Vallenari, A., et al. 2021, *A&A*, 649, A1
- Gallagher, J. S., & Starrfield, S. 1978, *ARA&A*, 16, 171
- Geballe, T. R., Banerjee, D. P. K., Evans, A., et al. 2019, *ApJL*, 886, L14
- Gehrels, N., Chincarini, G., Giommi, P., et al. 2004, *ApJ*, 611, 1005
- Gehrz, R. D., Evans, A., Helton, L. A., et al. 2015, *ApJ*, 812, 132
- Godon, P., Shara, M. M., Sion, E. M., & Zurek, D. 2017, *ApJ*, 850, 146
- Godon, P., Sion, E. M., Szkody, P., & Blair, W. P. 2020, *MNRAS*, 494, 5244

- Gordon, A. C., Aydi, E., Page, K. L., et al. 2021, *ApJ*, 910, 134
- Gutermuth, R. A., & Heyer, M. 2015, *AJ*, 149, 64
- Hachisu, I., & Kato, M. 2007, *ApJ*, 662, 552
- Hellier, C. 2001, *Cataclysmic Variable Stars*, ed. . Springer
- Helton, L. A., Gehrz, R. D., Woodward, C. E., et al. 2012, *ApJ*, 755, 37
- Henze, M., Pietsch, W., Haberl, F., et al. 2014, *A&A*, 563, A2
- Herbig, G. H., Preston, G. W., Smak, J., & Paczynski, B. 1965, *ApJ*, 141, 617
- Herter, T. L., Adams, J. D., Gull, G. E., et al. 2018, *Journal of Astronomical Instrumentation*, 7, 1840005
- Heywood, I. 2020, *oxkat: Semi-automated imaging of MeerKAT observations*, , ascl:2009.003
- Hillman, Y., Orio, M., Prialnik, D., et al. 2019, *ApJL*, 879, L5
- Hillman, Y., Shara, M. M., Prialnik, D., & Kovetz, A. 2020, *Nature Astronomy*, 4, 886
- Honeycutt, R. K., Robertson, J. W., & Kafka, S. 2011, *AJ*, 141, 121
- Honeycutt, R. K., Robertson, J. W., & Turner, G. W. 1995, *ApJ*, 446, 838
- Jonas, J., & MeerKAT Team. 2016, in *MeerKAT Science: On the Pathway to the SKA*, 1
- Kafka, S. 2020, *Observations from the AAVSO International Database*, <https://www.aavso.org>
- Kawash, A., Chomiuk, L., Strader, J., et al. 2021, *ApJ*, 910, 120
- Kenyon, S. J. 1986, *The symbiotic stars*
- Kim, S.-W., Wheeler, J. C., & Mineshige, S. 1992, *ApJ*, 384, 269
- Kniazev, A. Y., Gvaramadze, V. V., & Berdnikov, L. N. 2016, *MNRAS*, 459, 3068
- Kobulnicky, H. A., Nordsieck, K. H., Burgh, E. B., et al. 2003, in *Society of Photo-Optical Instrumentation Engineers (SPIE) Conference Series*, Vol. 4841, *Instrument Design and Performance for Optical/Infrared Ground-based Telescopes*, ed. M. Iye & A. F. M. Moorwood, 1634–1644
- Körding, E., Rupen, M., Knigge, C., et al. 2008, *Science*, 320, 1318
- Liller, W., Jacques, C., Pimentel, E., Aguiar, J. G. D. S., & Shida, R. Y. 2005, *IAUC*, 8596, 1
- Livio, M. 1992, *ApJ*, 393, 516
- Lomb, N. R. 1976, *Ap&SS*, 39, 447
- Long, K. S. 1996, in *IAU Colloq. 152: Astrophysics in the Extreme Ultraviolet*, ed. S. Bowyer & R. F. Malina, 301
- Mainzer, A., Bauer, J., Grav, T., et al. 2011, *ApJ*, 731, 53
- Mikołajewska, J. 2002, *MNRAS*, 335, L33
- Mikołajewska, J. 2003, in *Astronomical Society of the Pacific Conference Series*, Vol. 303, *Symbiotic Stars Probing Stellar Evolution*, ed. R. L. M. Corradi, J. Mikołajewska, & T. J. Mahoney, 9
- Mikołajewska, J., Friedjung, M., Kenyon, S. J., & Viotti, R., eds. 1988, *Astrophysics and Space Science Library*, Vol. 145, *The symbiotic phenomenon*
- Miller-Jones, J. C. A., Sivakoff, G. R., Altamirano, D., et al. 2011, in *Jets at All Scales*, ed. G. E. Romero, R. A. Sunyaev, & T. Belloni, Vol. 275, 224–232
- Mohamed, S., & Podsiadlowski, P. 2007, in *Astronomical Society of the Pacific Conference Series*, Vol. 372, *15th European Workshop on White Dwarfs*, ed. R. Napiwotzki & M. R. Burleigh, 397
- Monet, D. G., Levine, S. E., Canzian, B., et al. 2003, *AJ*, 125, 984
- Morales-Rueda, L., & Marsh, T. R. 2002, *MNRAS*, 332, 814
- Mroz, P., & Udalski, A. 2019, *The Astronomer’s Telegram*, 12876, 1
- Mukai, K., Orio, M., & Della Valle, M. 2008, *ApJ*, 677, 1248
- Munari, U. 2019, *arXiv e-prints*, arXiv:1909.01389
- Munari, U., Moretti, S., & Maitan, A. 2020, *A&A*, 639, L10
- Munari, U., Siviero, A., & Henden, A. 2005, *MNRAS*, 360, 1257
- Ness, J. U., Schwarz, G. J., Retter, A., et al. 2007, *ApJ*, 663, 505
- O’Donoghue, D., Buckley, D. A. H., Balona, L. A., et al. 2006, *MNRAS*, 372, 151
- Ogley, R. N., Chaty, S., Crocker, M., et al. 2002, *MNRAS*, 330, 772
- Osaki, Y. 1974, *PASJ*, 26, 429
- Otulakowska-Hypka, M., Olech, A., & Patterson, J. 2016, *MNRAS*, 460, 2526
- Page, K. L., Beardmore, A. P., & Osborne, J. P. 2020, *Advances in Space Research*, 66, 1169
- Patterson, J., Kemp, J., Harvey, D. A., et al. 2005, *PASP*, 117, 1204
- Pearson, K. J. 2006, *MNRAS*, 371, 235
- Ramsay, G., Schreiber, M. R., Gänsicke, B. T., & Wheatley, P. J. 2017, *A&A*, 604, A107
- Ricker, G. R., Winn, J. N., Vanderspek, R., et al. 2015, *Journal of Astronomical Telescopes, Instruments, and Systems*, 1, 014003
- Roming, P. W. A., Kennedy, T. E., Mason, K. O., et al. 2005, *SSRv*, 120, 95
- Russell, T. D., Miller-Jones, J. C. A., Sivakoff, G. R., et al. 2016, *MNRAS*, 460, 3720
- Sabbadin, F., & Bianchini, A. 1983, *A&AS*, 54, 393
- Saito, R. K., Hempel, M., Minniti, D., et al. 2012, *A&A*, 537, A107

- Salazar, I. V., LeBleu, A., Schaefer, B. E., Landolt, A. U., & Dvorak, S. 2017, *MNRAS*, 469, 4116
- Scargle, J. D. 1982, *ApJ*, 263, 835
- Schaefer, B. E. 2010, *ApJS*, 187, 275
- Schenker, K. 2002, in *Astronomical Society of the Pacific Conference Series*, Vol. 259, IAU Colloq. 185: Radial and Nonradial Pulsations as Probes of Stellar Physics, ed. C. Aerts, T. R. Bedding, & J. Christensen-Dalsgaard, 580
- Schwarz, G. J., Ness, J.-U., Osborne, J. P., et al. 2011, *ApJS*, 197, 31
- Schwarzenberg-Czerny, A. 2003, in *Astronomical Society of the Pacific Conference Series*, Vol. 292, Interplay of Periodic, Cyclic and Stochastic Variability in Selected Areas of the H-R Diagram, ed. C. Sterken, 383
- Seauquist, E. R., & Taylor, A. R. 1990, *ApJ*, 349, 313
- Seauquist, E. R., Taylor, A. R., & Button, S. 1984, *ApJ*, 284, 202
- Sekiguchi, K. 1992, *Nature*, 358, 563
- Shara, M. M., Livio, M., Moffat, A. F. J., & Orio, M. 1986, *ApJ*, 311, 163
- Shara, M. M., Prialnik, D., & Shaviv, G. 1977, *A&A*, 61, 363
- Shortridge, K., Meyerdierks, H., & Bridger, A. 1992, *Starlink System Note*, 40
- Skopal, A., Tomov, N. A., & Tomova, M. T. 2013, *A&A*, 551, L10
- Smak, J. 2000, *NewAR*, 44, 171
- . 2020, *AcA*, 70, 317
- Smith, A. J., Haswell, C. A., Murray, J. R., Truss, M. R., & Foulkes, S. B. 2007, *MNRAS*, 378, 785
- Sokoloski, J. L., Kenyon, S. J., Espey, B. R., et al. 2006, *ApJ*, 636, 1002
- Stahl, O., Kaufer, A., & Tubbesing, S. 1999, in *Astronomical Society of the Pacific Conference Series*, Vol. 188, Optical and Infrared Spectroscopy of Circumstellar Matter, ed. E. Guenther, B. Stecklum, & S. Klose, 331
- Starrfield, S., Truran, J. W., Sparks, W. M., & Kutter, G. S. 1972, *ApJ*, 176, 169
- Steiner, J. E., Cieslinski, D., Jablonski, F. J., & Williams, R. E. 1999, *A&A*, 351, 1021
- Stolz, B., & Schoembs, R. 1984, *A&A*, 132, 187
- Tody, D. 1986, in *Society of Photo-Optical Instrumentation Engineers (SPIE) Conference Series*, Vol. 627, Instrumentation in astronomy VI, ed. D. L. Crawford, 733
- Tokovinin, A., Fischer, D. A., Bonati, M., et al. 2013, *PASP*, 125, 1336
- Tomov, N., & Tomova, M. 2013, *Information Bulletin on Variable Stars*, 6055, 1
- Udalski, A., Szymański, M. K., & Szymański, G. 2015, *AcA*, 65, 1
- VanderPlas, J. T. 2018, *ApJS*, 236, 16
- Walter, F. M., Battisti, A., Towers, S. E., Bond, H. E., & Stringfellow, G. S. 2012, *PASP*, 124, 1057
- Wang, S., & Chen, X. 2019, *ApJ*, 877, 116
- Warner, B. 1995, *Cataclysmic variable stars*, Vol. 28
- . 2003, *Cataclysmic Variable Stars*, doi:10.1017/CBO9780511586491
- Webbink, R. F., Rappaport, S., & Savonije, G. J. 1983, *ApJ*, 270, 678
- Whitelock, P. A. 1987, *PASP*, 99, 573
- Wilber, A., Neric, M., Starrfield, S., Wagner, R. M., & Woodward, C. E. 2015, *The Astronomer's Telegram*, 7217, 1
- Wolf, W. M., Bildsten, L., Brooks, J., & Paxton, B. 2013, *ApJ*, 777, 136
- Yaron, O., Prialnik, D., Shara, M. M., & Kovetz, A. 2005, *ApJ*, 623, 398
- Young, E. T., Becklin, E. E., Marcum, P. M., et al. 2012, *ApJL*, 749, L17
- Zemko, P., Mukai, K., & Orio, M. 2015, *ApJ*, 807, 61
- Zemko, P., Orio, M., Mukai, K., et al. 2016, *MNRAS*, 460, 2744

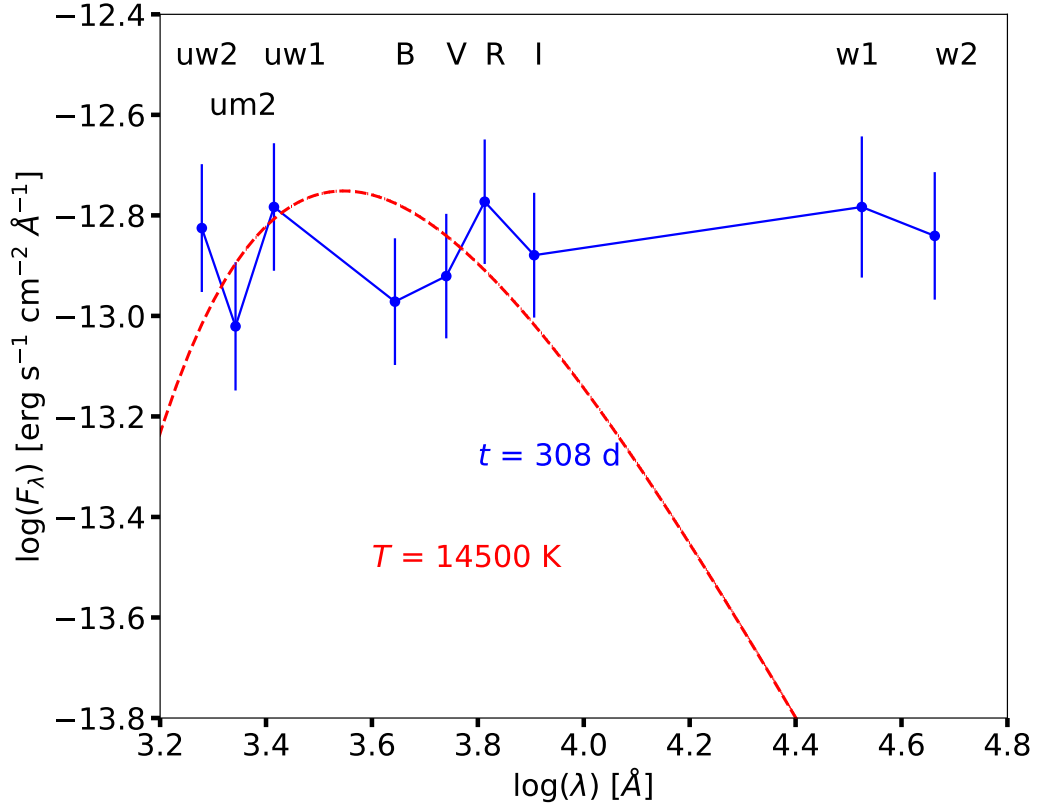


Figure A.1. Extinction-corrected SED plot, showing the UV to NIR SED of V1047 Cen on day 308. The error bars are 1σ uncertainties and they include contributions from the photometric and extinction uncertainties. The red-dashed curve represents the best fit blackbody model. The temperature quoted is derived from the best fit blackbody model.

APPENDIX

A. SUPPLEMENTARY PLOTS AND TABLES

In this Appendix we present supplementary plots and tables.

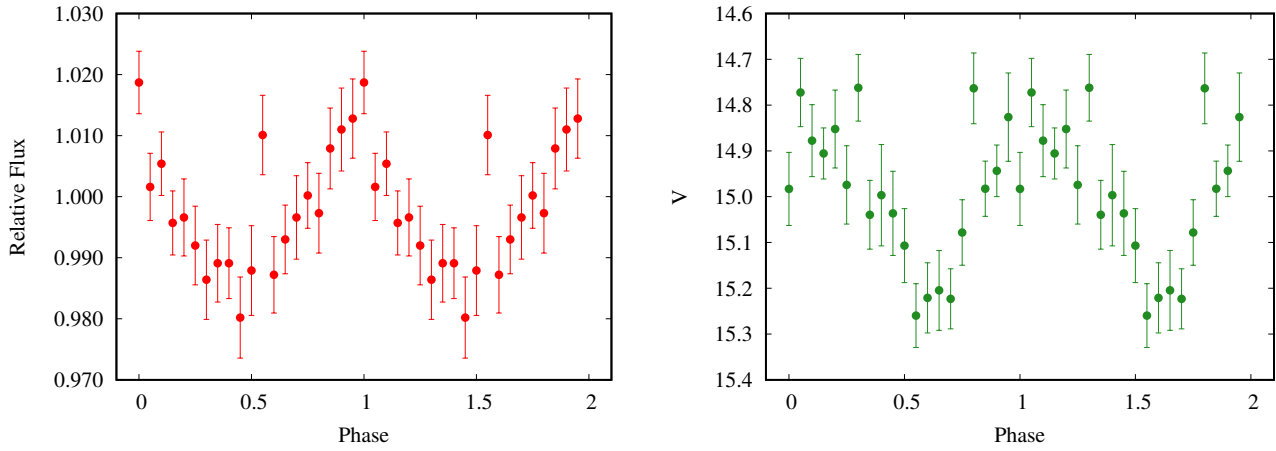


Figure A.2. The binned, phase-folded *TESS* (left) and AAVSO *V*-band (right) light curves, over the periods of 0.36 days (left) and 8.36 days (right), respectively.

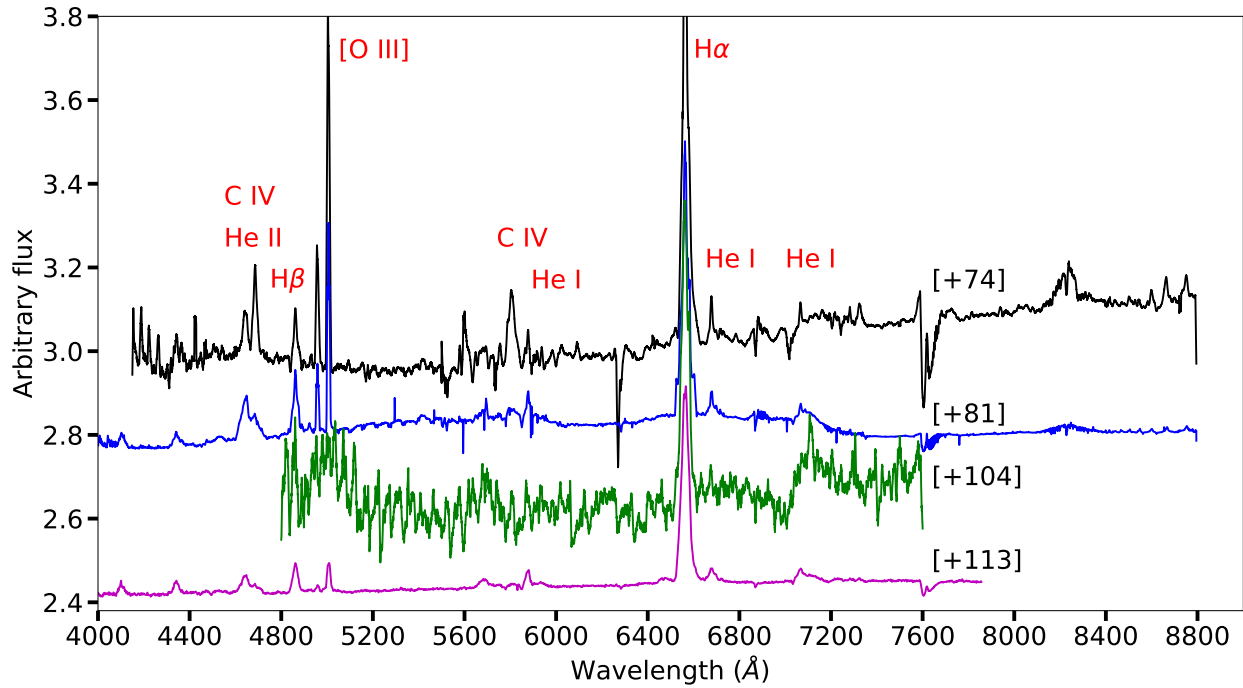


Figure A.3. The optical spectral evolution of V1047 Cen. The numbers in brackets are days since t_0 .

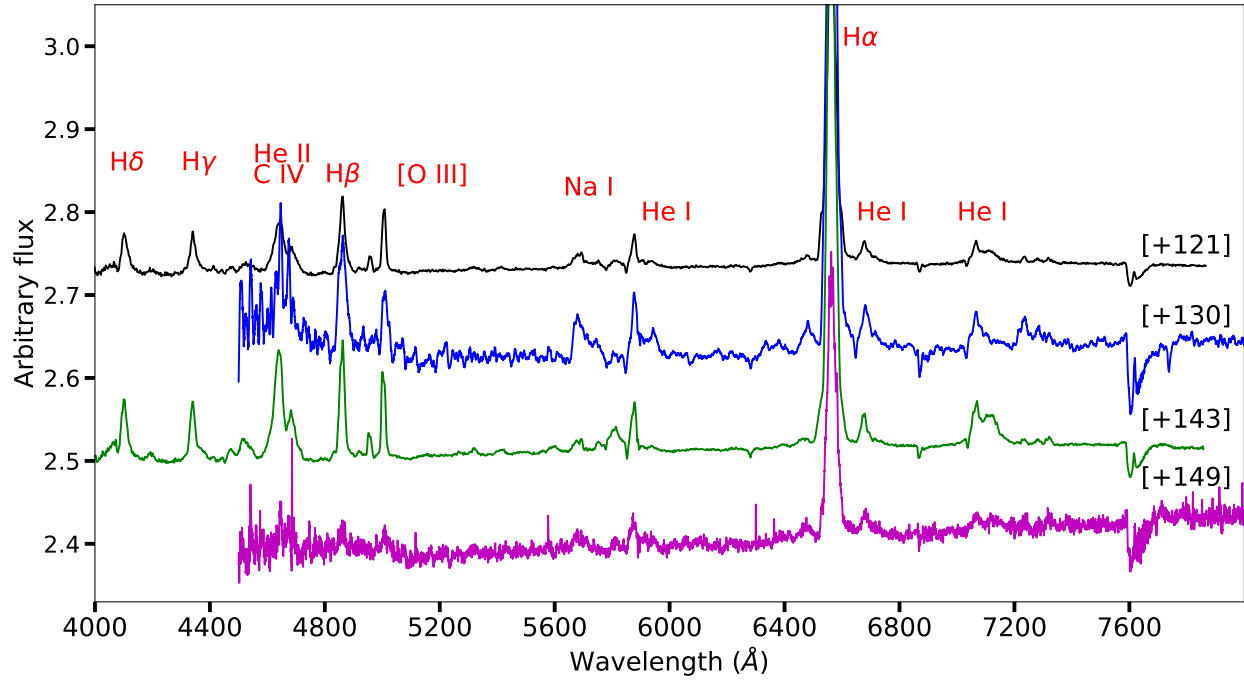


Figure A.4. The optical spectral evolution of V1047 Cen. The numbers in brackets are days since t_0 .

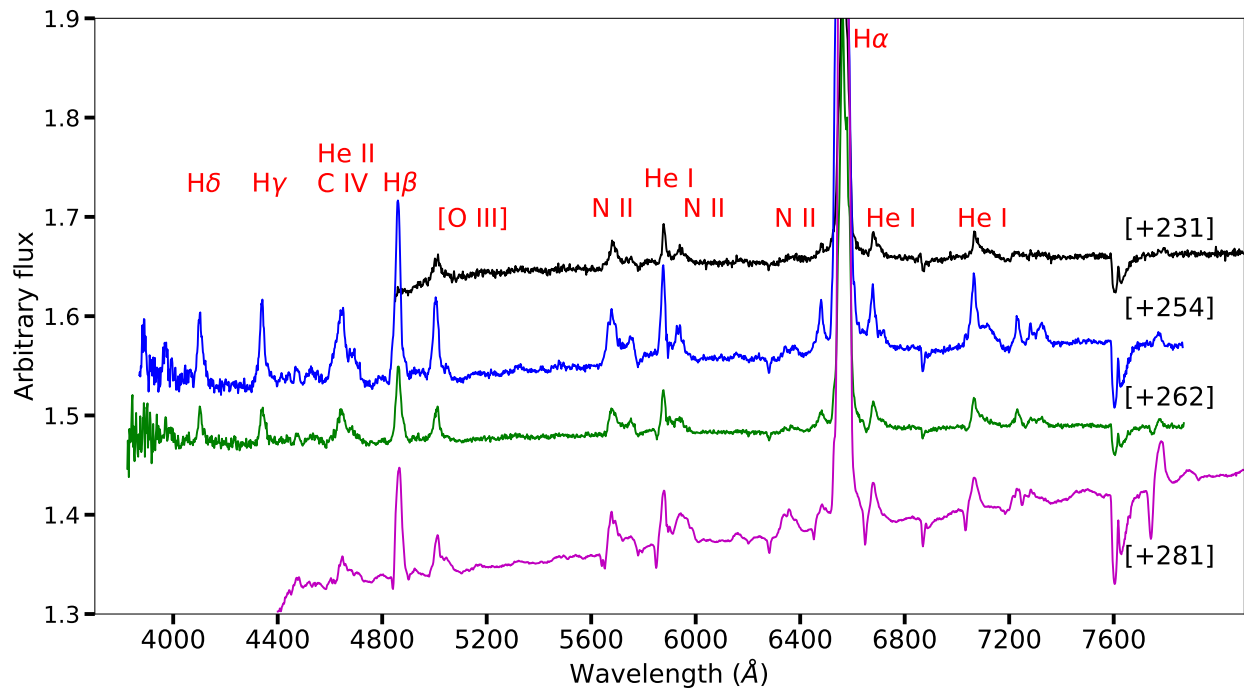


Figure A.5. The optical spectral evolution of V1047 Cen. The numbers in brackets are days since t_0 .

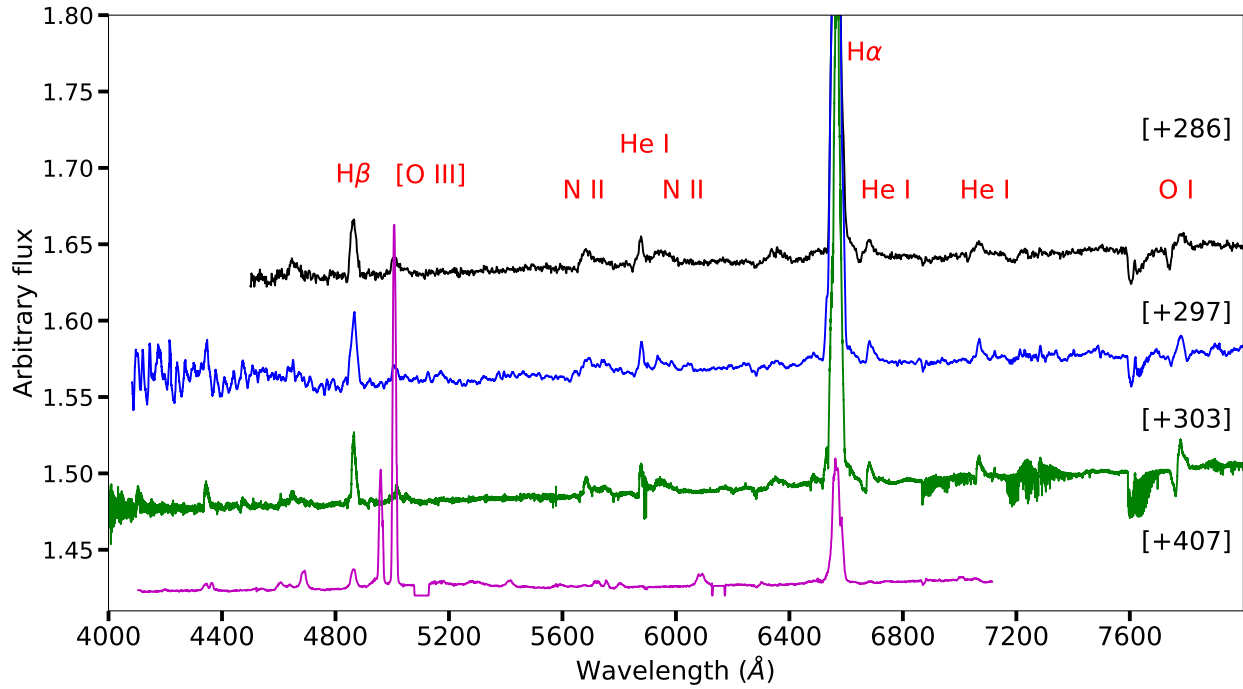


Figure A.6. The optical spectral evolution of V1047 Cen. The numbers in brackets are days since t_0 .

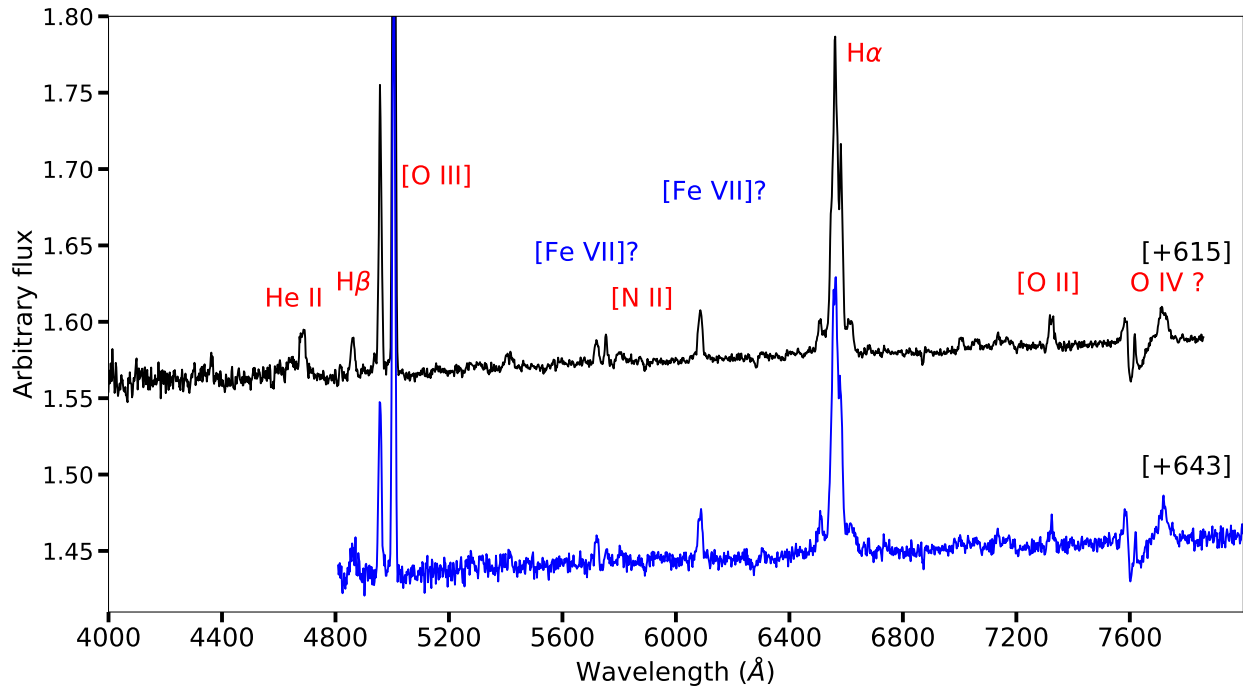


Figure A.7. The optical spectral evolution of V1047 Cen. The numbers in brackets are days since t_0 .

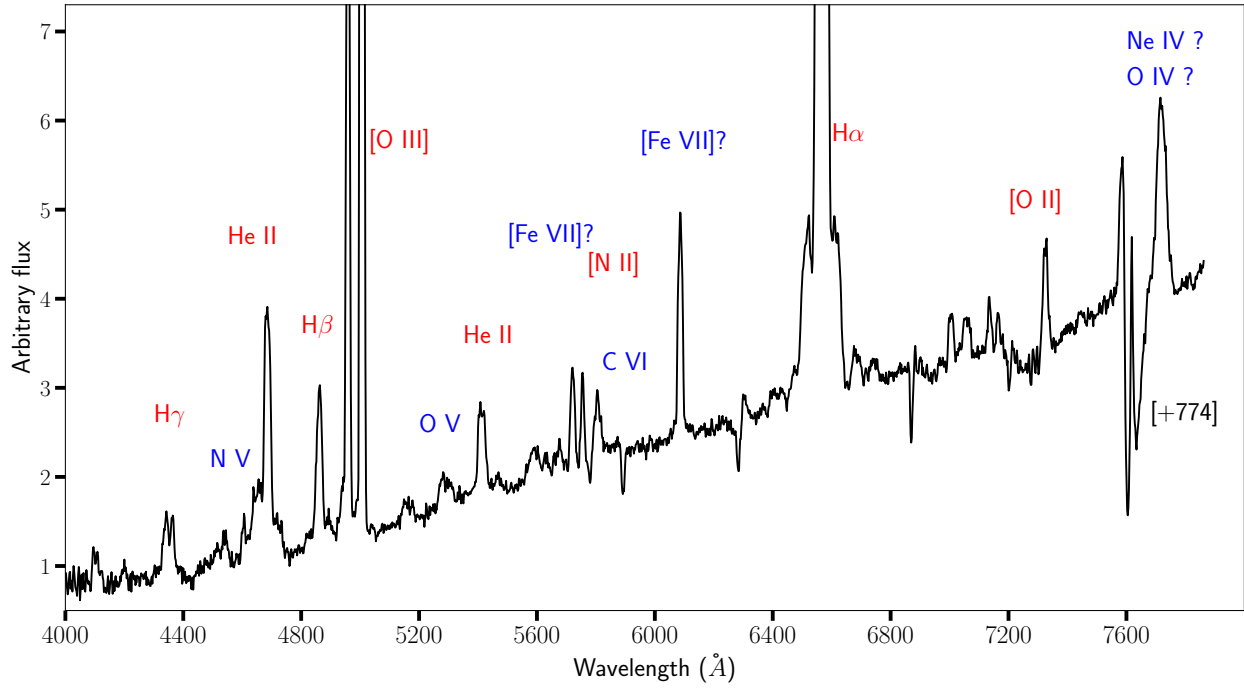


Figure A.8. The optical spectral evolution of V1047 Cen. The numbers in brackets are days since t_0 .

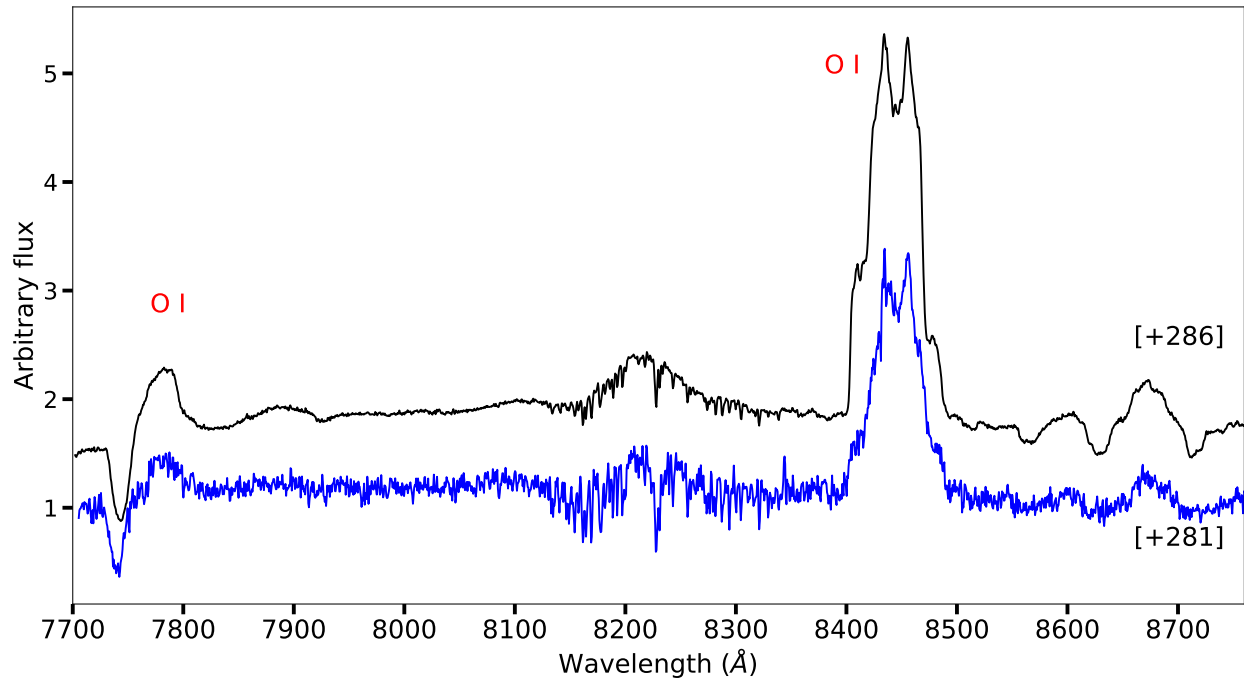


Figure A.9. The optical spectral evolution of V1047 Cen. The numbers in brackets are days since t_0 .

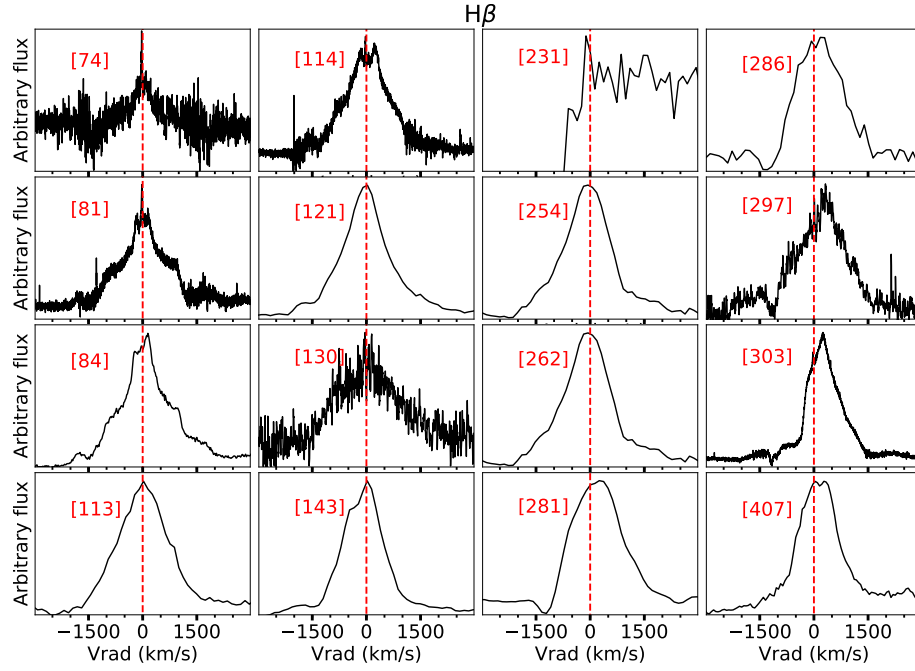


Figure A.10. The line profile evolution of H β throughout the outburst of V1047 Cen. The numbers between brackets are days after outburst. The red dashed lines represents the rest velocity ($V_{\text{vrad}} = 0 \text{ km s}^{-1}$). A heliocentric correction is applied to the radial velocities.

Table A.1. Log of the OGLE optical photometry.

JD	Magnitude	Err.	Band
2456437.64553	17.190	0.037	<i>I</i>
2456438.65480	17.325	0.040	<i>I</i>
2456465.62998	17.052	0.028	<i>I</i>
2456467.65411	17.075	0.033	<i>I</i>
2456478.47615	17.156	0.025	<i>I</i>
2456494.56288	17.111	0.043	<i>I</i>
2456500.50861	17.094	0.032	<i>I</i>
2456522.47809	17.061	0.036	<i>I</i>
2456693.83993	16.963	0.017	<i>I</i>
2456699.82818	17.020	0.020	<i>I</i>
2456702.84838	17.012	0.021	<i>I</i>
2456705.81657	16.981	0.027	<i>I</i>
2456713.85601	17.076	0.021	<i>I</i>

Table A.2. Log of the AAVSO optical photometry.

JD	Magnitude	Err.	Band
2458655.4927	15.488	0.032	<i>V</i>
2458655.4938	15.503	0.026	<i>V</i>
2458655.4947	13.807	0.033	<i>I</i>
2458655.4954	13.846	0.038	<i>I</i>
2458655.4962	14.672	0.029	<i>R</i>
2458655.4970	14.636	0.030	<i>R</i>
2458656.4909	15.472	0.049	<i>V</i>
2458656.4911	16.674	0.065	<i>B</i>
2458656.4920	15.475	0.036	<i>V</i>
2458656.4929	13.718	0.051	<i>I</i>
2458656.4936	13.709	0.040	<i>I</i>
2458656.4945	14.542	0.032	<i>R</i>
2458656.4952	14.531	0.030	<i>R</i>
2458656.4963	16.497	0.056	<i>B</i>
2458656.4977	16.468	0.058	<i>B</i>

Table A.3. Log of the SMARTS NIR photometry.

JD	Magnitude	Err.	Band
2458656.49902	12.265	0.016	<i>H</i>
2458656.50000	11.864	0.018	<i>K</i>
2458656.50000	13.014	0.025	<i>J</i>
2458657.51172	11.465	0.019	<i>K</i>
2458657.51172	11.967	0.013	<i>H</i>
2458657.51172	12.682	0.027	<i>J</i>
2458657.51562	12.057	0.012	<i>H</i>
2458657.51660	11.602	0.018	<i>K</i>
2458657.51660	12.735	0.025	<i>J</i>
2458660.50195	11.327	0.018	<i>K</i>

Table A.4. Log of the NEOWISE NIR photometry.

JD	Magnitude	Err.	Band
2458685.13	9.224	0.092	<i>W1</i>
2458685.13	8.382	0.083	<i>W2</i>
2458887.15	8.368	0.083	<i>W1</i>
2458887.15	7.741	0.074	<i>W2</i>
2458894.82	8.585	0.085	<i>W1</i>
2458894.82	7.998	0.079	<i>W2</i>
2459049.28	12.119	0.121	<i>W1</i>
2459049.28	10.737	0.107	<i>W2</i>

Table A.5. Optical spectroscopic observations log.

Telescope	Instrument	date	$t - t_0$ (days)	Resolving power	λ Range (Å)
SALT	HRS	2019-06-19	74	14000	4000–9000
SALT	HRS	2019-06-26	81	14000	4000–9000
SOAR	Goodman	2019-06-29	84	5000	4500–5170
SOAR	Goodman	2019-06-29	84	5000	6130–6710
SMARTS	CHIRON	2019-07-17	104	28000	4080–8900
SOAR	Goodman	2019-07-28	113	1000	3800–7800
SOAR	Goodman	2019-07-28	113	5000	6130–6710
SALT	HRS	2019-07-29	114	14000	4000–9000
SOAR	Goodman	2019-08-05	121	1000	3800–7800
SOAR	Goodman	2019-08-05	121	5000	6130–6710
SMARTS	CHIRON	2019-08-14	130	28000	4080–8900
SOAR	Goodman	2019-08-27	143	1000	3800–7800
SOAR	Goodman	2019-08-27	143	5000	6130–6710
SMARTS	CHIRON	2019-09-02	149	28000	4080–8900
SOAR	Goodman	2019-11-23	231	1000	3800–7800
SOAR	Goodman	2019-11-23	231	5000	6130–6710
SOAR	Goodman	2019-12-16	254	1000	3800–7800
SOAR	Goodman	2019-12-16	254	5000	6130–6710
SOAR	Goodman	2019-12-24	262	1000	3800–7800
SOAR	Goodman	2019-12-24	262	5000	6130–6710
SOAR	Goodman	2020-01-12	281	1000	3800–7800
SOAR	Goodman	2020-01-12	281	2800	7700–8870
SOAR	Goodman	2020-01-12	281	5000	6130–6710
SOAR	Goodman	2020-01-17	286	1000	3800–7800
SOAR	Goodman	2020-01-17	286	2800	7700–8870
SOAR	Goodman	2020-01-17	286	5000	6130–6710
SMARTS	CHIRON	2020-01-28	297	28000	4080–8900
SALT	HRS	2020-02-03	303	14000	4000–9000
SALT	RSS	2020-05-17	407	1500	4100–7200
SOAR	Goodman	2020-11-12	615	1000	3800–7800
SOAR	Goodman	2021-01-08	643	1000	3800–7800

Table A.6. Gemini South / Flamingos 2 Observations of V1047 Cen.

Date	$t - t_0$ (days)	Wavelength (μm)	R_{max} $\lambda/\Delta\lambda$	Integration (s)	airmass (mean)	standard star
2020-02-23	323	1.17–1.30	3,000	1200	1.64	(a)
2020-02-23	323	1.49–1.78	3,000	1200	1.52	HIP63036
2020-02-23	323	1.95–2.45	3,000	1200	1.42	HIP63036
2020-03-01	330	0.89–1.75	1,200	120	1.63	HIP63036

^aSpectra of HIP63036 and HIP67360 combined to match airmass of V1047 Cen.

Table A.7. Log of MeerKAT radio observations at 1.28 GHz.

Date	MJD	$(t - t_0)$	Peak flux (mJy beam ⁻¹)	Int. flux ^a (mJy)	α
2019-11-26	58813.18	234.07	0.93 ± 0.06	0.95 ± 0.08	0.1 ± 0.1
2019-12-15	58832.40	253.29	0.88 ± 0.06	0.92 ± 0.08	0.0 ± 0.1
2019-12-20	58837.44	258.33	0.89 ± 0.07	0.9 ± 0.1	0.5 ± 0.2
2019-12-28	58845.28	266.17	0.93 ± 0.06	0.90 ± 0.08	1.0 ± 0.2
2020-01-03	58851.41	272.30	0.81 ± 0.05	0.88 ± 0.08	–
2020-01-10	58858.42	279.31	0.78 ± 0.05	0.89 ± 0.08	0.8 ± 0.5
2020-01-20	58868.21	289.10	0.87 ± 0.06	0.78 ± 0.07	0.2 ± 0.3
2020-01-25	58873.18	294.07	0.80 ± 0.04	0.91 ± 0.06	0.2 ± 0.2
2020-02-01	58880.29	301.18	0.89 ± 0.05	0.86 ± 0.07	–
2020-02-08	58887.20	308.09	0.84 ± 0.05	0.82 ± 0.07	0.6 ± 0.3
2020-02-15	58894.16	315.05	0.76 ± 0.05	0.83 ± 0.07	0.1 ± 0.2
2020-02-21	58900.25	321.14	0.81 ± 0.05	0.79 ± 0.08	1.5 ± 0.2
2020-03-02	58910.16	331.05	0.75 ± 0.04	0.93 ± 0.06	–0.2 ± 0.2
2021-03-06	59279.20	700.09	0.91 ± 0.05	0.91 ± 0.07	–0.09 ± 0.1

^aIntegrated flux at 1.28 GHz, calculated by fitting a Gaussian to V1047 Cen and integrating the Gaussian’s flux. Spectral indices were derived by imaging in eight frequency channels, fitting a point source in each sub-band image, and fitting the resulting fluxes with a power-law. We assume a 10% flux calibration error for the flux in each sub-band, while a 5% flux calibration error is assumed for the full band flux measurement.

Table A.8. Log of the *Swift* UVOT photometry.

JD	Magnitude	Err.	Band
2458659.1322	17.533	0.084	<i>uvw1</i>
2458688.9402	17.525	0.080	<i>uvw1</i>
2458703.2580	16.927	0.068	<i>uvw1</i>
2458659.1284	19.492	0.281	<i>uvm2</i>
2458703.2548	18.816	0.188	<i>uvm2</i>
2458709.9321	18.564	0.159	<i>uvm2</i>
2458718.3840	18.099	0.179	<i>uvw2</i>
2458722.2083	18.415	0.122	<i>uvw2</i>
2458731.7276	18.178	0.126	<i>uvw2</i>